# The Prevention of Crack Propagation in Metal Alloy by Laser Remelting


Author

USAMA BILAL

Regn Number

00000203997

Supervisor

Dr. MUSHTAQ KHAN

DEPARTMENT OF DESIGN & MANUFACTURING ENGINEERING

SCHOOL OF MECHANICAL & MANUFACTURING ENGINEERING

NATIONAL UNIVERSITY OF SCIENCES AND TECHNOLOGY

ISLAMABAD



JULY, 2020

# The Prevention of Crack Propagation in Metal Alloy by Laser Remelting

Author

USAMA BILAL

Regn Number

00000203997

A thesis submitted in partial fulfillment of the requirements for the degree of

MS Design & Manufacturing Engineering

Thesis Supervisor:

Dr. MUSHTAQ KHAN

Thesis Supervisor's Signature: _____

DEPARTMENT OF DESIGN & MANUFACTURING ENGINEERING

SCHOOL OF MECHANICAL & MANUFACTURING ENGINEERING

NATIONAL UNIVERSITY OF SCIENCES AND TECHNOLOGY,

ISLAMABAD

JULY, 2020

# Declaration

I certify that this research work titled "*The Prevention of Crack Propagation in Metal Alloy by Laser Remelting"* is my own work. The work has not been presented elsewhere for assessment. The material that has been used from other sources it has been properly acknowledged / referred.

Signature of Student

USAMA BILAL

2020-NUST-Ms-DME-00000203997

## Plagiarism Certificate (Turnitin Report)

This thesis has been checked for Plagiarism. Turnitin report endorsed by Supervisor is attached.

Signature of Student
USAMA BILAL
Registration Number
00000203997

Signature of Supervisor

## Proposed Certificate for Plagiarism

It is certified MS Thesis Titled The Prevention of Crack Propagation in Metal Alloy by Laser Remelting by Usama Bilal has been examined by us. We undertake the follows:

a. Thesis has significant new work/knowledge as compared already published or are under consideration to be published elsewhere. No sentence, equation, diagram, table, paragraph or section has been copied verbatim from previous work unless it is placed under quotation marks and duly referenced.
b. The work presented is original and own work of the author (i.e. there is no plagiarism). No ideas, processes, results or words of others have been presented as Author own work.
c. There is no fabrication of data or results which have been compiled/analyzed.
d. There is no falsification by manipulating research materials, equipment or processes, or changing or omitting data or results such that the research is not accurately represented in the research record.
e. The thesis has been checked using TURNITIN (copy of originality report attached) and found within limits as per HEC plagiarism Policy and instructions issued from time to time.

**Name & Signature of Supervisor**

**Dr. Mushtaq Khan**

**Signature:** _____

## Thesis Acceptance Certificate

Certified that final copy of MS thesis written by Mr. Usama Bilal, (Registration No 00000203997), of SMME has been vetted by undersigned, found complete in all respects as per NUST Statutes/Regulations/MS Policy, is free of plagiarism, errors and mistakes and is accepted as partial fulfillment for award of MS degree. It is further certified that necessary amendments as pointed out by GEC members and foreign/local evaluators of the scholar have also been incorporated in the said thesis.

Signature with Stamp: _____

Name of Supervisor: Dr. Mushtaq Khan

Date: _____

Signature of HoD with Stamp: _____

Date: _____

**Countersign By**

Signature (Dean/Principal): _____

Date: _____

**FORM TH-4**

# National University of Science & Technology

## MASTER THESIS WORK

We hereby recommend that the dissertation prepared under our supervision by: (Student Name & Regn No.) Usama Bilal 00000203997 Titled: The Prevention of Crack Propagation in Metal Alloy by Laser Remelting be accepted in partial fulfillment of the requirements for the award of MS Design & Manufacturing Engineering degree. (Grade___)

**Examination Committee Members**

1. Name: Dr. Syed Husain Imran Signature:_____

2. Name: Dr. Najam ul Qadir Signature:_____

Supervisor's name: Dr. Mushtaq Khan Signature:_____

Date:_____

Dr. Mushtaq Khan
Head of Department

_____
Date

**COUNTERSINGED**

Date:_____

_____
Dean/Principal

## Copyright Statement

## Acknowledgements

I am very thankful to Allah Almighty to guide me throughout the research process and make me understand and gain the knowledge of various fields, so indeed none be worthy of praise but You.

I am profusely thankful to my beloved parents who have helped me and support me financially and emotionally throughout my thesis work.

I would also like to express special thanks to my supervisor Dr. Mushtaq Khan for his help throughout my thesis as guidance to fulfill my aims of thesis and providence of required Mechanical Facilities inside or outside of the NUST.

I would like to thank my GEC members for giving me the right direction in successfully achieving my goals. I am thankful to Dr. Husain Imran for helping me design the experiments and Dr. Najmul Qadir for making me understand the knowledge of material sciences.

I would also like to pay special thanks to Dr. M. Mujahid for his tremendous support and cooperation in teaching me the concepts of chemical, materials and metallurgy and for the availability of labs in SCME.

I would also like to thank Mr. Nadeem Mehdi of HMC Taxila for providing the material, Dr. Rehan for providing the laser facilities to conduct laser experiments and Mr. Toheed for the nano hardness in GIKI.

Finally, I would like to express my gratitude to all the individuals in lab facilities who have rendered valuable assistance to my study.

# Dedication

Dedicated to my parents, siblings, uncle and advisors whose tremendous support and cooperation led me to this wonderful accomplishment.

## Abstract:

There were many methods previously used to repair the cracks, induced during fatigue loading. The most commonly used was hole drilling method and then insertion of pins to increase the fatigue performance. Another method involving laser shockwave peening had been used to treat the surface cracks. The method similar to laser shockwave peening was studied in the present research, which comprises of laser remelting. The method was analyzed as a crack preventing technique. The laser re-melting scans were performed on a steel plate by varying the energy density and defocusing of the laser.. The samples were sectioned perpendicular to the laser scan and the cut surface was polished to a mirror finish using metallographic techniques including mounting, grinding and polishing. The microstructure was revealed by etching the polished surface that clearly exposed the grains structure in the optical microscope. The focus point of the laser beam was identified by the microstructural study of the samples. Hardness testing was performed to analyze the trend of the hardness throughout the sample including the base metal, HAZ and melt-zone. Moreover, toughness was ascertained through the microstructural analysis that showed as grain size variations and phase changes. The microstructure toughness was considered to be the most crucial factor in analyzing the prevention strategies of fatigue crack propagation.



**Key Words:** *Crack Propagation, Fatigue Loading, Laser Remelting, Nano Hardness, Micro Hardness, Microstructural Analysis.*

# Table of Contents

# List of Figures

# List of Tables

# CHAPTER 1: INTRODUCTION

## 1.1 Problem Statement

The prevention of crack propagation in metal alloy by laser remelting.

## 1.2 Introduction

Fatigue failure occurs when a material is subjected to cyclic stress. The number of stress cycles to initiate crack and to propagate till the fracture, determines the fatigue life of a material. The failure in fatigue has three stages; initiation of crack, crack propagation and rapid fracture. The fatigue crack is normally initiated at the point of highest stress concentration. Therefore, the surface condition of the material plays an important role in fatigue life [1].

The repairs for fatigue crack becomes important in sustaining the damage and increasing the fatigue life. There has been several fatigue cracks repairing method, which involves processes like grinding, gas tungsten arc remelting, air hammer peening, ultrasonic impact treatment, hole drilling, adding doubler plates and post tensioning. Traditionally, hole drilling has been most commonly used to stop the crack at the vicinity of its tip [2].

Moreover, laser shockwave peening was used as surface treatment method to treat surface cracks. The high energy laser plastically deforms the material and develop compressive residual stress inside the material [3]. Laser remelting process, used in the present work, is similar to laser shockwave peening that intends to refine the grains and homogenize alloy distribution in the material in order to improve resistance against crack propagation [4].

## 1.3 Objectives

The objectives were following:

- To determine the focus point of the laser beam
- To achieve maximum melt pool depth for crack prevention.
- To study the hardness of laser processed area of the material
- To study the microstructure of the laser processed material
- To achieve better microstructure toughness in the laser processed area
- To increase the fatigue life of a cracked material
- To prevent crack propagation
- To shorten the time for repairing
- To ease the process of repairing

## 1.4 Scope

The scope of the present research is following:

- Crack repairing of in service applications
- To ease the crack repairing process as compare to the conventional process
- Time reduction for the repairing process
- To increase the service life of the material

## 1.5 Flow Chart

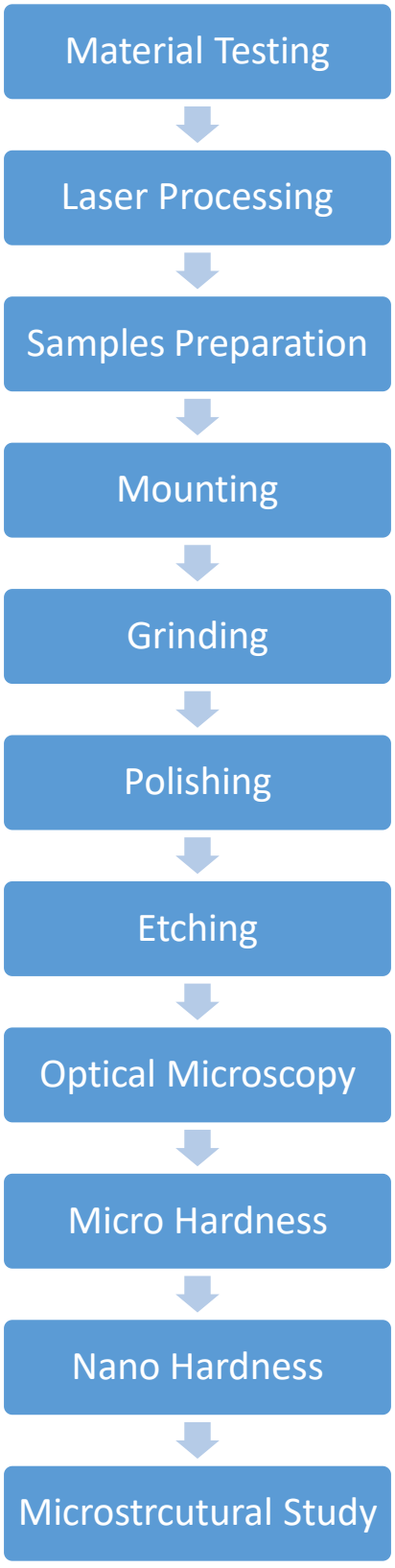

# CHAPTER 2: LITERATURE REVIEW

Fatigue is one of the primary reasons that cause failure of metallic components in a number of applications. The fatigue failure is caused by the cyclic loading of a material. The process involves continuous loading and unloading of force on a material that causes the crack to initiate at the stress concentration points and then leads it to its fatigue failure. There are following three stages for fatigue failure at the application of cyclic loading [1]:

- Crack Initiation
- Crack Growth
- Rapid Fracture

The continuous loading and unloading of force led to crack nucleation and crack initiation. The continuation of that force resulted in progressive growth of a crack known as crack propagation until the remaining un-cracked cross section of a material became too weak to sustain the loads imposed and the material suddenly fractures [1].

Repairing and retrofit techniques can be used for fatigue crack arresting and upgrading its resistance to fatigue. Repairs are used to stop the propagation of a fatigue crack while retrofit upgraded the resistance to fatigue to avoid fatigue crack initiation and propagation. Retrofits techniques are performed at the same conditions that cause the cracks in the first place [2].

There are several repairing and retrofit methods that could be considered to be effective in preventing the crack including surface treatments, repair of through-thickness cracks and modifications of structure [2].

The surface treatments comprise of grinding, gas tungsten arc re-melting (GTA re-melting) of weld toe and impact treatments. These treatments provide the improvement in fatigue life as following [2]:

- Improvements in weld geometry and reduction in stress concentration
- Elimination of severe discontinuities which propagate cracks
- Reducing residual tensile stress
- Introducing compressive residual stress

## 2.1 Grinding [2]

It is a surface treatment method of reshaping by grinding. It is used to remove the small cracks, like cracks at the edges of flange or plates. The tapering of 2.5:1 slope should be applied to counter gouge and finish grinding should be done parallel to the applied cyclic stresses.

The grinding was not considered to be useful in terms of micro cracks because it produces defects in the material, which resembles to the initial micro cracks. The reshaping by burr grinder was observed to have 50% more allowable fatigue stress range as compared to its untreated parts. There are two types of grinders that can be used for material removal.

### 2.1.1 Disc Grinding

Disc Grinding is a process which involves the material removal in one pass of the grinder. The typical grinding discs are made up of Aluminum Oxide having 24-grit roughness, ranges from 4 - 9 inches (101- 230 mm) in diameter. The depth of ground area should be in range of 2-5% of plate thickness. The excess of the material removal can be avoided with care. The operator should be in control of grinder to avoid the risk of producing gouges.

**Figure 1:** Typical Disc Grinders [2]

Figure 1 shows the two disc grinders that are typically used in the material removal.

### 2.1.2 Burr Grinder

Burr grinder is used for removing material from confined areas. The typical burr grinder is made up of Tungsten Carbide with a radius of 3/16 – 5/16 inch (4.7 – 8mm). The method is easy to handle and recommended for grinding edge of welds and enlarging small drill holes.

**Figure 2:** Typical Burr Grinder with different tips

Figure 2 shows the typical burr grinder with different carbide tips.

## 2.2 Gas Tungsten Arc (GTA) Re-melting [2]

It is a welding operation along the weld toe and the base material. It involves re-melting by manually moving a gas shielded tungsten electrode at a constant speed along the weld toe and just melting the metal without addition of new filler metal. It removes slag intrusions and reduced stress concentration at the weld toe which helps in preventing the crack.

## 2.3 Impact Treatments [2]

These introduce compressive residual stress near the weld toe which reduce the effective tensile stress range at the crack surface.

## 2.4 Air Hammer Peening [2]

It was a weld improvement technique that uses an air hammer with a blunt tip to plastically deform the weld toe. It also created the compressive residual stress on the points where tensile stress was produced during a welding process. It decreased the tensile stress range at the weld toe under live load which leads to the extension of fatigue life and it adds the shinier glow to the surface being treated.

The fatigue life of welds was improved by air hammer peening even when there were no detectable fatigue cracks because it introduced the residual compressive stress. The compressive residual stress depth ranged from two to four times the plastically deformed grain depth, i.e. from 0.04-0.08 inches (1-2 mm) deep.

Peening has been demonstrated to be useful in repairing surface cracks up to a depth of 0.12-inch (3 mm). The improvement of up to 175% in the fatigue resistance of welds repair was expected by air hammer peening. The elimination of crack like defects or blunting defects like slag inclusion improved fatigue resistance of a material [5].

**Figure 3:** Air hammer peened weld toe [2]

Figure 3 shows the weld toe which was Air hammer peened. The geometry and luster can be seen at weld toe.

## 2.5 Ultrasonic Impact Treatment [2]

The more attractive, quiet and easy to handle impact treatment was ultrasonic impact treatment as compare to the air hammer peening. It used low amplitude and high frequency displacements. It was also a more effective treatment in improving the fatigue strength than the air hammer peening by at least one detail category [6]. This treatment had more effectiveness at low mean stresses and low stress ranges.

## 2.6 Hole Drilling [2]

The most commonly used method for the repairing of fatigue cracks was hole drilling. The purpose was to eliminate the sharp notch of the crack tip by drilling a hole at the vicinity of crack tip. The hole was required to be of sufficient size to detain the crack. The large sized holes were better as long as they did not compromise the stiffness and strength of the material. The typical range of the hole was 2-4 inches (50.8 – 101.6mm) but hole diameter of 1 inch (25.4mm) was sufficient depending upon the application.

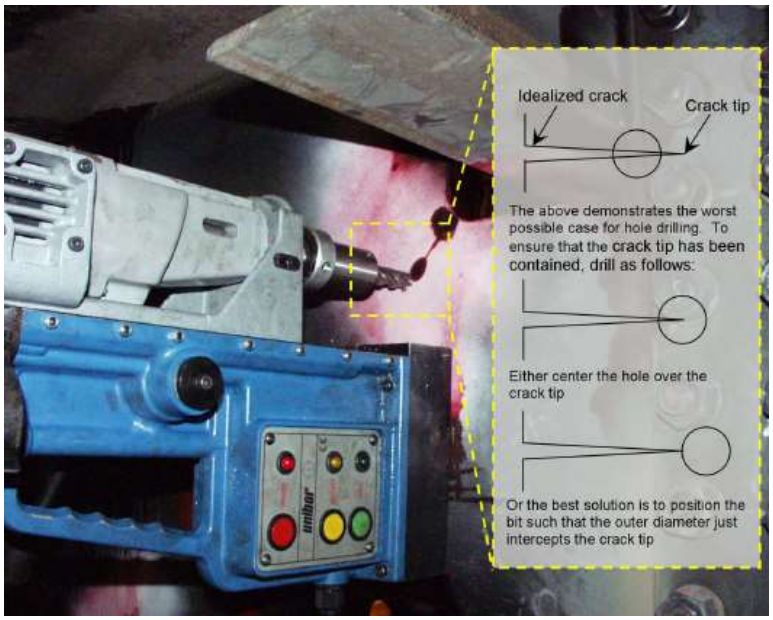


**Figure 4:** Hole Drilling Method [2]

Figure 4 shows the hole drilling method at the vicinity of crack tip. It also represents three different ways which can be used to drill a hole.

The study of drilling a stop holes on Aluminum Alloy near the vicinity of the crack tip was studied. The stop holes were drilled in different arrangements to reduce the stress concentration and then pins were inserted into those holes to introduce the compressive residual stress. The symmetric and asymmetric arrangements of holes were demonstrated [7].

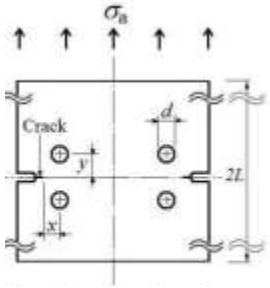


**Figure 5:** Symmetric 4 Holes Arrangement [8]

Figure 5 shows the symmetric arrangement of four holes which provided the best results without insertion of pins and with insertion of pins. The x and y in the figure 5 represents the distance from x-axis and y-axis respectively. The d represents diameter of the hole, $\sigma_a$ represents the applied stress and L represents the length of the sample in the figure 5. The direction of the applied stress was presented by arrows in the figure 5. The fatigue life was increased 20 times as compare to its untreated counter parts. The process was terminated at certain stress cycles due to the shortage of time [7].

The stop holes drilling method with and without inserting pins was not able to work for arresting long cracks. The patch was installed at the stop holed area to arrest long cracks for simple shaped structures. The crack arrestor was used with the stop holes to arrest the long cracks for complicated shape structures. The crack arrester reduced the crack opening displacement [7].

## 2.7 Vee and Weld [2]

It was a repairing method for long and thorough thickness cracks in the weld. The material was removed in the shape of the V, through three quarter thickness of the cracked section in the direction of the crack length. The weld material was filled in the V-shaped groove. This process was performed on the other side of the section so that weld filled the whole area of the crack.

The air arc gouging or grinding can be used for material removal. The crack became blurred when a disc grinder was used to remove the material and it increased the chances of covering the crack path and left a flaw in the repair weld while air arc gouging opened up the crack as the material was removed and crack path was easily followed.

**Figure 6:** Air arc gouged flange of a beam for Vee and Weld Repair [2]

Figure 6 shows the flange of a beam which was air arc gouged for a Vee and Weld Repair. The repair method was used for high strength steel when bolted doubler method was not possible. The method required a care in the quality of weld made on the V-shaped grooves. The certified and experienced welders can be used to ensure the quality of the weld to be up to standard. It was considered to be the most effective technique of repairing a weld crack. It has provided the same fatigue life as the original uncracked weld. The repairing of base metal without any weld through vee and weld was considered to be insignificant. It was expected to provide less fatigue life as compare to the original unwelded detail.

## 2.8 Adding Doubler/Splice Plates [2]

The cracks of through thickness can be repaired by doubler or splicer plates. Its purpose was to add material to a cracked cross section. It has provided either continuity or increased the cross section. It also reduced the stress ranges that originally led the material to crack. The doubler plates can be added after the repair to decreases the stress range that originally cracked the material.

The plates were designed to have more thickness to avoid buckling effect and maintained the alignment of both sides. It was useful to repair the full depths crack in bridge girder. The splice plates were attached by welding or through high strength bolt. The bolted doubler plates were preferred over welded doubler plates for a better fatigue resistance.

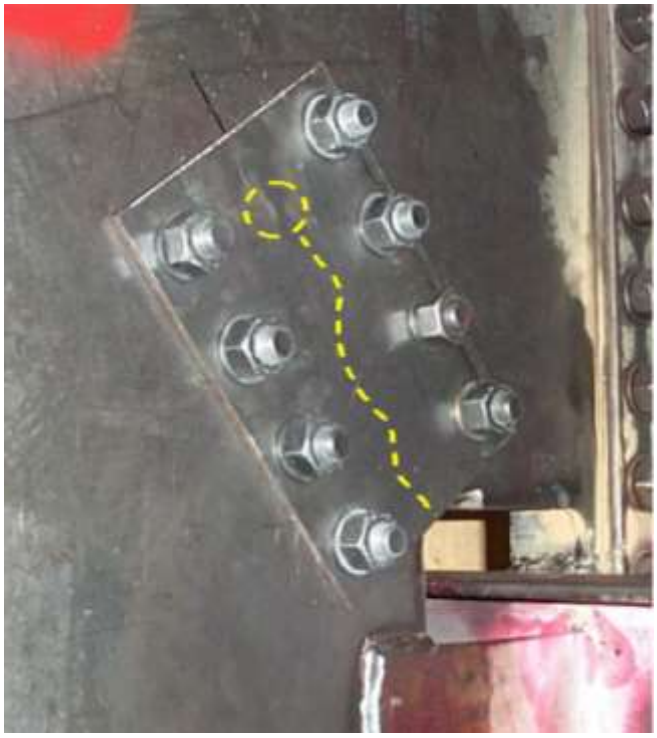

**Figure 7:** Bolted Doubler Plate Repair [2]

Figure 7 shows the doubler plate repair which was attached by the bolts. The yellow dotted line represents the path of the crack below doubler plate and circle shows the hole drilled to eliminate the tip of the crack. The steel material conforms to AASHTO M270 was used for the repair. The bolts conform to ATM 325 or 490 standards and washers conform to ASTM F436.

## 2.9 Post Tensioning [2]

The fatigue crack growth can be slowed or stopped by the concept of closure of a crack. The post tensioning forces were used on the cracked beam section to force the closure of the cracked faces together and to push the effective stress range into the regime of compression to disturb additional crack propagation. The crack growth was hindered by the compressive stress range.

The study showed that the application of post tensioning force with pre-stressing strands on the cracked plate detail increased the fatigue strength of repaired section by one category more than the original detail. The elimination of crack tip by hole drilling was recommended with post tensioning force. It can be applied by jacking pre-stressing strands, post tensioning bars or by nuts that can be torqued on high strength threaded rods.

## 2.10 Laser Shockwave Peening (LSP) [3, 8]

It is a surface treatment technique which is used for improving fatigue strength of the material that has cracks at the surface. It is used for metals and alloys due to its capability of generating large affected depths and a good surface. The residual stress and plastic strain is predicted by studying the effects of shockwave, induced by high energy laser.

The study was conducted in which solid state Nd:glass laser with a wavelength of 1.054 µm and a pulse duration of 18 ns was used as a laser source with a power density of 5 GW/cm$^2$. The sacrificial layer of thin black paint layer was used to absorb energy. The plasma confinement layer of thin water layer was used to contain the plasma that was created by high energy laser beam.

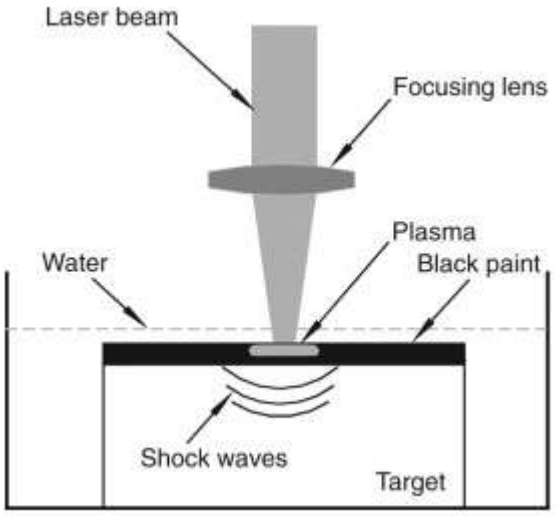


**Figure 8:** Schematic of Laser Shockwave Peening (LSP) [8]

Figure 8 shows the schematic of laser shockwave peening. The high energy pulsed laser beam absorbed in the sacrificial layer (water), creates plasma that is confined in the plasma confined layer (black paint) It penetrated inside the material as shockwaves to plastically deform the material below the surface. The residual compressive stress was developed throughout the affected depth.

The X-ray Diffraction technique was used to measure the residual stress. It decreased with increasing depth and the maximum residual compressive stress of 380MPa has been recorded on the 2024 T3 Aluminum alloy. The depth of penetration was observed as approximately 1mm. The typical depth of penetration in conventional peening was 0.25mm.

The LSP method showed significant improvement in fatigue performance of Aluminum alloy. The crack initiation life and fatigue life was observed to be higher in the laser peened specimen as compare to its unpeened counterparts. The slow crack growth rate was also observed due to less fatigue striations spacing in laser peened specimen as compare to unpeened specimen. It attributed

to the introduction of residual compressive stress. The fatigue life was improved by slow crack growth rate and introduction of compressive residual stress.

## **2.11** Hot Rolling Effect on Microstructure of Steel **[9]**

The multi pass hot rolling is used in the temperature range of 700-1000 ˚C. The microstructure of a hot rolled nitrogen alloyed austenitic stainless steel was analyzed in optical microscope. The elongation of grains in rolling direction, nucleation and growth of new grains at grain boundary of elongated grains were observed in optical microscope to form completely recrystallized grains. The insufficient temperature for dynamic recrystallization resulted in elongation of grains at temperature range of 700-800 ˚C while fine grains were observed at the temperature range of 900-1000 ˚C to achieve dynamic recrystallization.

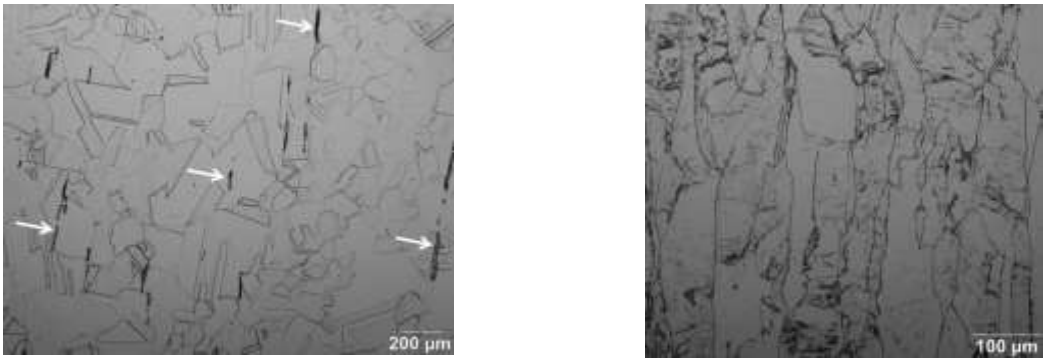


(b) (b)

**Figure 9:** Optical Microscopic image of microstructure of the nitrogen alloyed stainless steel a) annealed condition b) hot rolled condition [9]

Figure 9 shows the optical microscopic image of microstructure of the nitrogen alloyed stainless steel with annealed condition in its part (a) and with hot rolled condition in its part (b). The annealed sample has austenitic grains with annealing twins of average grain size 120 $\pm$ 15 µm and phase of 0.6% delta ferrite (showed by arrows) in the part (a) of the figure 9. The grains of the hot rolled steel were elongated at the temperature of 700 ˚C. The elongated grains have been observed to have length of 213 ± 60 µm and width of 56 ± 22 µm.

## 2.12 Laser Surface Remelting [10]

In this study, laser surface remelting was performed on the bainitic steel with the help of fiber laser. It was used to improve the strength and wear resistance of the surface of material. The transmission electron microscopy (TEM) was used to study the microstructure of the laser processed specimen. The effect of scanning speed and scanning space was analyzed on the microstructure and hardness of the surface remelted material. The fiber laser with a spot size of 0.1 mm and wavelength in the range of 1060 – 1100 nm was used to surface treat the material. The argon as a shielding gas has been used in the process to protect the laser melt pool by reducing the oxidation and evaporation of material.

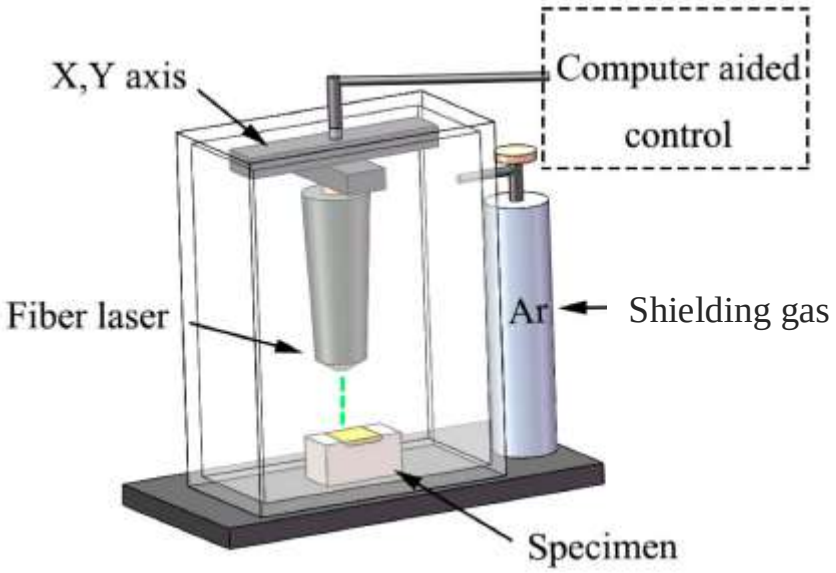


**Figure 10:** Schematic of Fiber Laser Surface Remelting [10]

Figure 10 shows the schematic of the laser surface remelting, which was performed by fiber laser with a shielding gas of Argon. The x and y axis movement of the laser has been controlled by the computer. The specimen with different scan speeds has provided different melt pool depths. The melt pool depth has been increased by decreasing the scan speed. The maximum melt pool depth was recorded as 138 microns. The microstructure of the samples was studied by TEM after grinding, polishing and etching. The grinding was performed on P240, P400 and P600, then polished with 2.5 W polishing paste. The samples was etched by 4% nital solution for 5 seconds to reveal the microstructure.

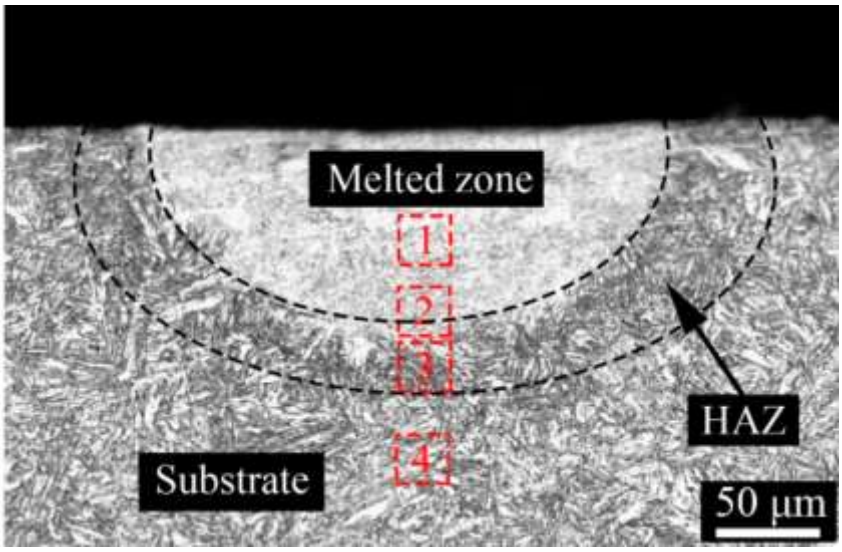


**Figure 11:** Microstructure of the laser single-pass modified cross sectional layer. [10]

Figure 11 represents the cross sectional microscopic image of the laser single pass modified layer. The complete and incomplete transformation can be seen in the figure 11. Martensite has been formed at the rapid cooling areas. The martensite formation was incomplete in the subsurface layer due to improper austenitization in heating. The figure 11 has four different points from 1 to 4, starting from melted zone and ending in substrate. The point 1 shows the martensite formation, which was caused by rapid heating and cooling. The point 2 shows the transformation of uniform lathe martensite into acicular martensite. The large acicular martensite can be observed in the HAZ region at point 3 in the figure 10 due to high residence time at high temperature. The point 4 has mixed microstructure of lathe bainite and martensite.

The nano hardness test showed that the laser modified layer has more hardness as compare to the BM and decreases from the surface to the inside of melted zone. The distance of 50 µm far from the surface showed the maximum hardness value of 6.8 GPa. The microstructure of fine lathe martensite has the maximum value of hardness of 6.8 GPa at the distance of 50 µm far from the surface. The hardness changes were found to be consistent with the results of microstructural analysis. The wear resistance of 55% compared with the matrix was increased by varying the laser parameters i.e. scan speed and scan spacing.

## 2.13 Hardness Trend of Solidification Process [11]

Rockwell C (HRC) hardness test was conducted on the AISI 204 stainless steel pipe, which was welded at 700 °C with a filler metal. The hardness was analyzed against different zones of the welded pipe; base material, heat affected zone, interface and weld zone. The hardness value has increased in the heat affected zone (HAZ) as compare to the base material. The hardness value decreased from the interface towards the center of the weld zone.

## 2.14 Effects of Grain Refinement and Microstructure on Fracture Toughness

### **2.14.1** Grain Refinement **[12]**

The fracture toughness of welded pressure vessel steel has been studied in terms of microstructure and grain size. Different cooling rates have provided different microstructure of welded heat affected zone. The air quenching of low temperature austenitization (LTA) specimen was observed to show better fracture toughness due to smaller grains size as compared with the base metal.

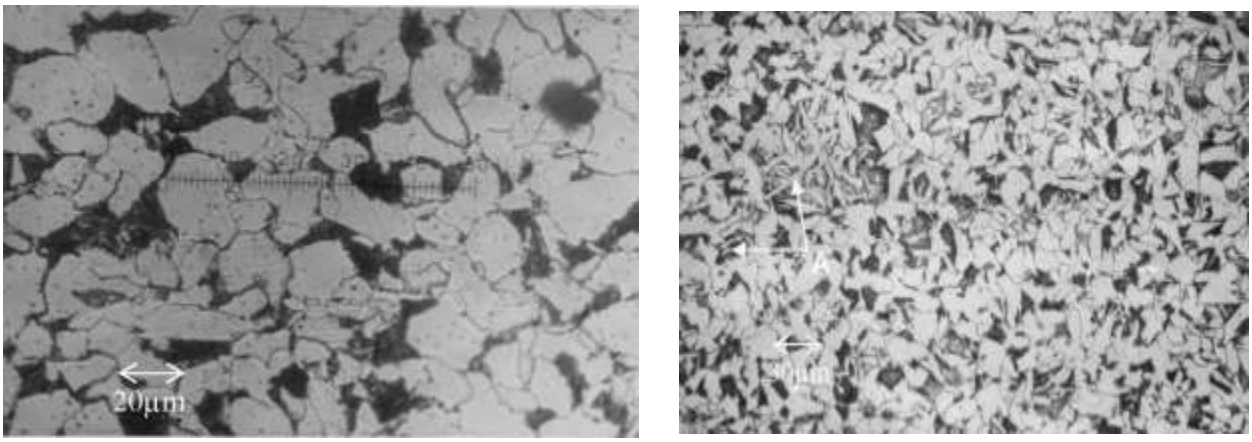


(a) (b)

**Figure 12:** Microstructure of Steel a) untreated steel b) LTA 925 [12]

Figure 12 shows the microstructure of Steel. The untreated steel is shown in (a) and low temperature austenitization (LTA) at 925 ˚C in (b) of the figure 12. The refinement of grain size in order of 19-28 µm was observed at the austenization of 975 ˚C as compare to the grain size of untreated material of 42 µm. The LTA at 975 ˚C showed higher toughness ($\delta_c$) of 0.264 mm as compare to the fracture toughness ($\delta_c$) of the base material of 0.187 mm.

### **2.14.2 Microstructural Changes**

#### **2.14.2.1 Ferrite and Pearlite [13]**

The microstructure of ferrite has body centered cubic (alpha) iron morphology in iron alloys like steel. The alpha ferrite is formed by cooling of austenite at slow rate, which rejects the carbon by diffusion. It is formed at the temperature range of 900°C to 723°C and is clearly visible at the room temperature. The delta ferrite is the form of iron, which is formed at high temperatures. The delta ferrite can only be retained at room temperature in highly alloyed steels.

The pearlite microstructure is formed at slow cooling of iron alloys in the temperature range of 1150 ˚C –723 ˚C. It has been observed to contain ferrite and cementite ($Fe_3C$). The ferrite and cementite grows during cooling of decomposing austenite through carbon atoms diffusion. The carbon separates as $Fe_3C$ between ferrite layers to form pearlite structure.

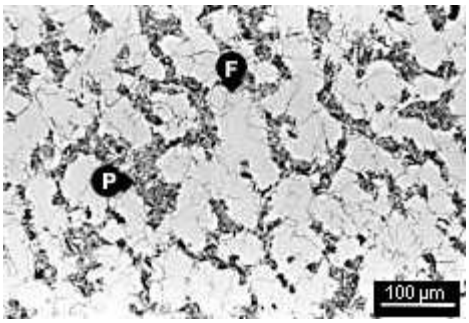


**Figure 13:** Alpha Ferrite (F) and Pearlite (P) [13]

Figure 13 shows the microstructure of iron carbon alloy with alpha ferrite and pearlite. The carbon solubility in iron decreases on cooling from austenite. The slow cooling results in carbide formation while fast cooling would trap the carbon in the crystal lattice.

### 2.14.2.2 Martensite [13]

The metastable martensite microstructure is formed in the steels, when austenite is cooled rapidly. The carbon is trapped in the crystalline ferrite, which increases hardness of the microstructure. There was no diffusion of carbon atoms in martensitic formation. The martensite start temperature could have a range from 500˚C to below room temperature. The range of martensite start temperature to finish temperature is typically 150 ˚C for low carbon steels.

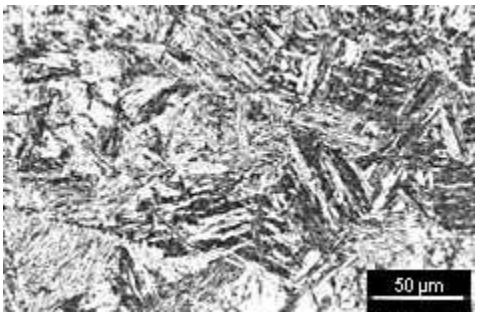


**Figure 14:** Martensite Microstructure [13]

Figure 14 shows the microstructure of martensite. The block and packet size of martensite controls the toughness and strength of the martensitic steel. The refinement of austenite grain size decreases the packets and block sizes of martensite, which improves the toughness of the material. Another method to reduce the packet and block size is used to decrease the cooling rate encouraging the partial formation of bainite before martensite transformation. The refinement of grains leads to better microstructural toughness [12, 14].

### 2.14.2.3 Bainite [13]

The microstructure of bainite is been formed in between the temperature of formation of ferrite and martensite from austenite. It has two types; upper bainite and lower bainite. Upper bainite is formed at the temperature range of 550 ˚C – 400 ˚C. The fine bainite laths are observed in the low carbon steels, which were formed due to shear at austenite grain boundaries. The carbon is pushed in the austenite surrounded by bainitic ferrite laths due to low solubility of carbon in bainitic ferrite. The high concentration of carbon in austenite nucleates the cementite particles at austenite/ferrite interface.

The microstructure is known as feathery bainite due to its pearlite like appearance. Lower bainite is formed at the temperature range of 400 ˚C – 250 ˚C. The carbon composition in steel defines the temperature of upper and lower bainite formation. It nucleates by partial shear like upper bainite. There is short range diffusion of carbon atoms, which give way to carbide formation 50 – 60˚ longitudinal to main lath adjacent with bainitic ferrite. The lower bainite appeared like martensitic structure.

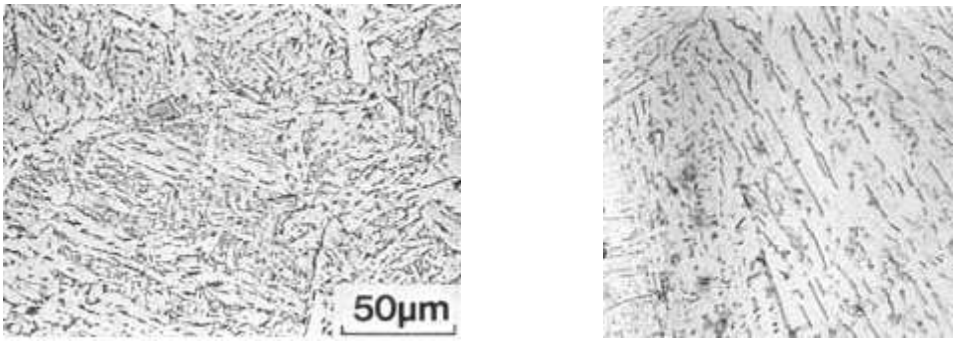


(a) (b)

**Figure 15:** Mictrostructure of Bainite a) Upper Bainite b) Lower Bainite [13]

Figure 15 shows the bainitic microstructure of upper bainite in part (a) and lower bainite in part (b). The bainite microstructure has packets of parallel plates [15]. The high density of high angled boundaries of bainite were observed to show good microstructural toughness [16]. The high angled boundaries are an obstacle for a cleavage crack to propagate, forcing the crack to change its microscopic plane of propagation to adjust new crystals [17].

Fracture toughness is an essential property of materials, which indicates the capacity of absorbing strain energy of a material before fracture. The high resistance to crack propagation can be achieved by high toughness of a material. The refined grain size and reduced quantity of intermetallic particles at the grain boundaries is observed to improve the fracture toughness of the metal alloys [18, 19].

# CHAPTER 3: EXPERIMENTATION AND METHODOLOGY

## 3.1 Material

The material used in the present research was hot rolled carbon steel plate, which conforms to the ASTM standard A516/A516M Grade 70. This steel was mostly used for manufacturing of pressure vessels and boilers [20]. The material was tested and had following chemical composition and mechanical properties:

**Table 1:** Chemical Composition (in wt. %)

| C (%) | Mn (%) | P (%) | S (%) | Si (%) | Cr (%) | Ni (%) | Mo (%) | Cu (%) |
|---|---|---|---|---|---|---|---|---|
| 0.16 | 0.84 | 0.024 | 0.014 | 0.05 | 0.35 | 0.002 | 0.01 | 0.007 |

**Table 2:** Mechanical Properties [20]

| Yield Strength (MPa) | Ultimate Tensile Strength (MPa) | Elongation (%) in 2in. (50mm) |
|---|---|---|
| 260 | 550 | 21 |

## 3.2 Terminologies

The following terminologies are used in the research:

**Table 3:** Attributes and Terminologies

| Attributes | Terminologies |
|---|---|
| Base Material | BM |
| Heat Affected Zone | HAZ |
| Melt Pool | MP |
| Energy Density | ED/E.D |
| Defocus | DF/D.F |

## 3.3 Laser Remelting

The Solid State laser; Neodymium-doped Yttrium Aluminum Garnet (Nd:YAG) Laser was used for the remelting of a material.

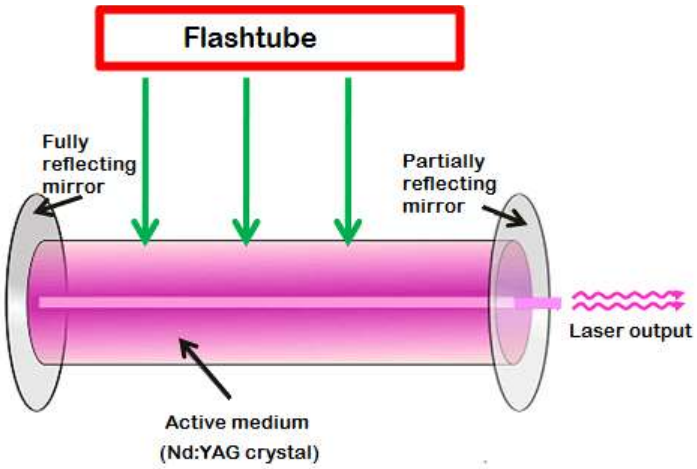


**Figure 16:** The Schematic of Nd:YAG Laser [21]

Figure 16 shows the schematic of Nd:YAG laser. It shows three main components; energy source, active/laser medium and optical resonator [21]. The energy source was to supply energy to the active medium by flashtube or laser diodes. The active medium in the laser was Nd:YAG crystal. The optical resonator was consisted of two mirror; fully silvered and partially silvered. The fully silvered mirror completely reflected the light. The partially silvered mirror partially reflected the light but some light passed through it to produce laser beam.

The Nd:YAG laser was used to produce scan lines on the material having different parameters. The basic parameters varied in the laser scans were defocusing of laser and laser energy density of a laser. The defocusing was varied to find the focus point of the laser by analyzing the melt pool depth and kerf width. The laser energy density was varied at focus point of the laser to analyze the melt pool depth and kerf width.

$$Laser\ Energy\ Density\ (J/mm^3) = \frac{laser\ power\ (J/s)}{laser\ spot\ size\ (mm) \times scan\ speed\ (mm/s)} \quad (1)$$

Equation 1 shows the equation of laser energy density [22]. It has a direct relation with the laser average power and inverse relation with the laser spot size and scan speed. The scan speed was varied by keeping laser spot size and average power constant to vary the laser energy density The laser scans were made on the material by keeping energy density constant and changing the defocus of the laser then laser scans were made on the material by keeping the defocus constant at the focus point and changing the laser energy density.

### 3.3.1 Design of Experiment (DOE)

**Table 4:** Design of Experiment (DOE)

| Sr. No. | Energy Density ($J/mm^3$) | Defocus (mm) |
|---|---|---|
| 1 | 300 | 0 |
| 2 | 300 | 2 |
| 3 | 300 | 4 |
| 4 | 300 | 8 |
| 5 | 300 | 10 |
| 6 | 75 | 2 |
| 7 | 150 | 2 |
| 8 | 300 | 2 |
| 9 | 600 | 2 |

### 3.3.2 Laser Scans

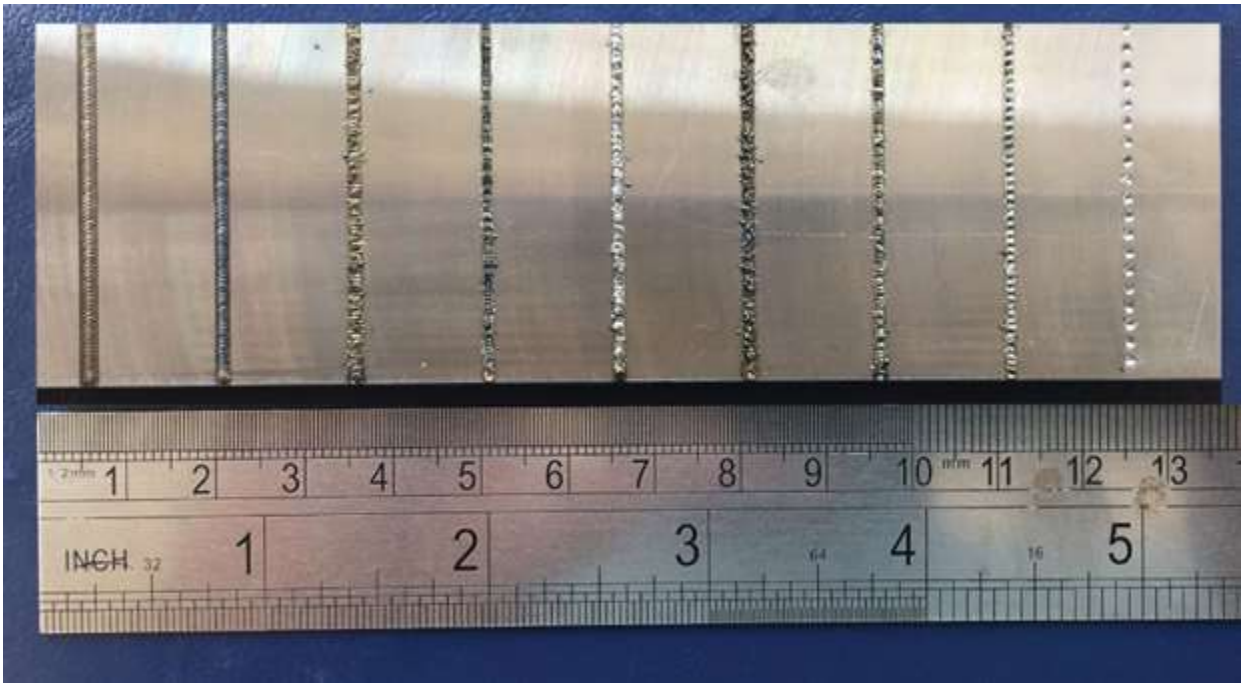


**Figure 17:** Laser Remelting Scans on a Steel Plate

Figure 17 represents the laser remelting scans on a 8mm thick steel plate of (136mmX48mm) size. There were total of nine laser scans. The first five scans from left to right in the figure 17 were performed by keeping the energy density constant at 300 $J/mm^3$ while changing the defocus of the laser beam. The next four scans in the figure 17 were performed by

keeping defocus constant at 2mm while changing the energy density of the laser beam. The melt pool depth, kerf width and effect of laser parameters on the microstructure are discussed later.

## 3.4 EDM Wire Cutting

The steel plate with laser scans was cut into samples by EDM wire cutting. The cutting was done in such a way that the heat affected zone created by EDM cutting did not affect the heat affected zone generated by laser re-melting. This can be confirmed later in the microstructural analysis of the laser treated samples.

The program was fed in the control unit of the machine to cut the rectangular samples from the steel plate. The wire of diameter 0.18mm was used to cut these samples. The total of 9 samples were cut through the plate. The dielectric fluid was directed at tool and workpiece which helped in initiating electric spark and also worked as a coolant for workpiece and wire.

**Figure 18:** EDM Wire Cutting Machine [23]

Figure 18 shows the EDM wire cutting machine used in the cutting process. There is a control unit on the left in the figure 18 which was used to feed the program for cutting and to control the motion of the machine's bed along x and y-axis. The unit on the right side of the figure 18 consists of servo mechanism, bed for workpiece and tool containing mechanism. The servo mechanism was controlled by control unit to control cutting current, feed rate and wire speed. The

workpiece was manually loaded on the bed. The program was fed on the control unit to control the movement of the bed during the cutting process. The conducting wire was used as a tool for the removal of material by electric spark.

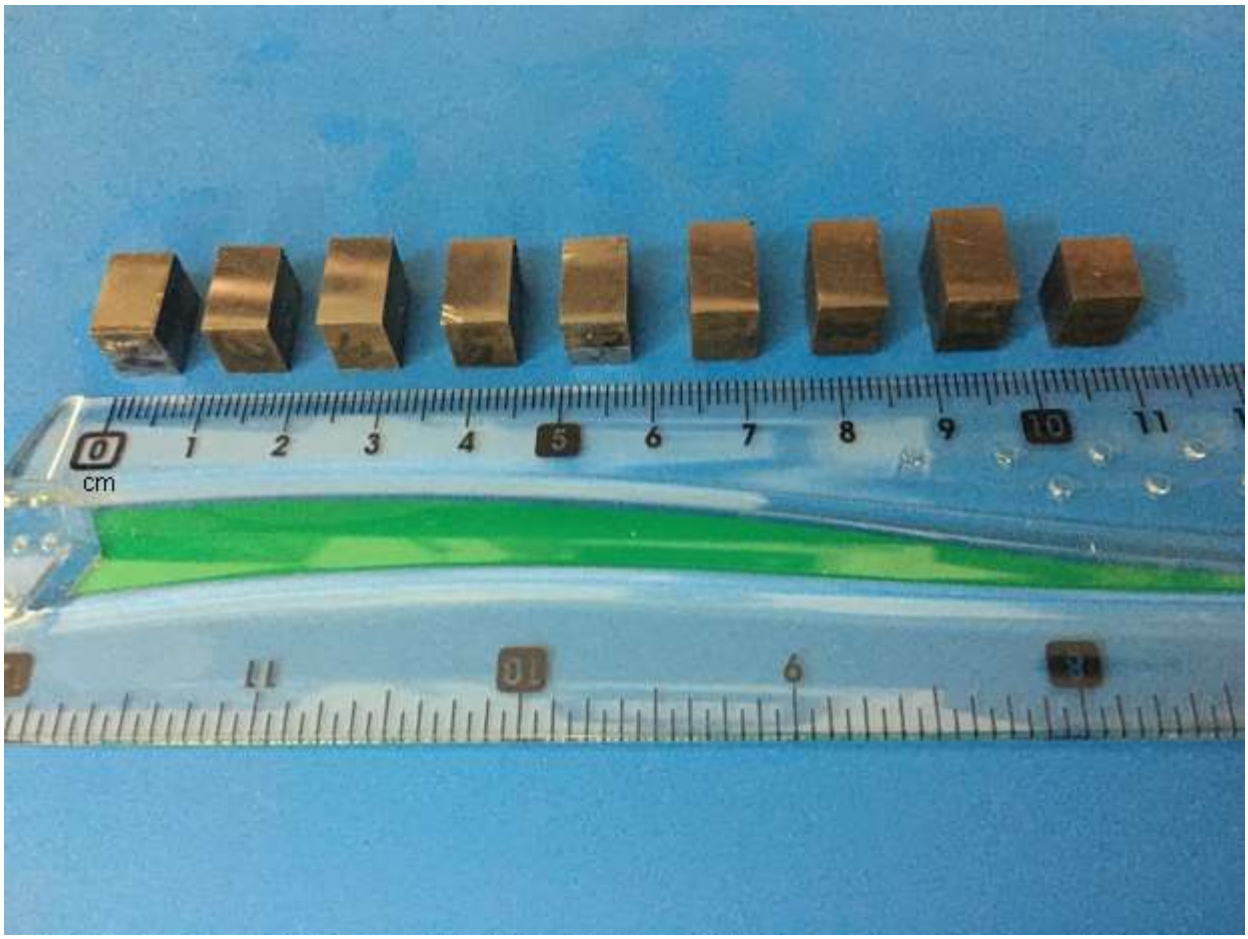


**Figure 19:** EDM Wire Cut Samples

Figure 19 shows the laser treated samples cut from the steel plate by EDM wire cutting. These samples were cut to do the microstructural analysis and observed the effects of laser re-melting on the microstructure of the samples.

## 3.5 Mounting

The samples cut by EDM wire cutting were mounted by hydropress automatic mounting. These mounted samples were fed into automatic grinding and polishing machine for grinding and polishing of samples to reduce surface roughness.

The conductive Bakelite powder was used to mount the samples in hydro-press. The side which needed to be analyzed was kept on top when placing the sample on the circular plate of the hydro-press. The machine was run for approximately 30-40 minutes to mount one sample.


**Figure 20:** Automatic Mounting Hydropress Machine

Figure 20 shows the Automatic Mounting Hydropress Machine. The display in the figure 21 shows the conditions which were used for the mounting of the samples. The sample was placed on the circular piston of the hydropress and the mounting material was poured onto it in the powder form. The hydropress used the hydraulic pistons to compact that powdered mounting material into a solid form disc with a sample mounted inside it.

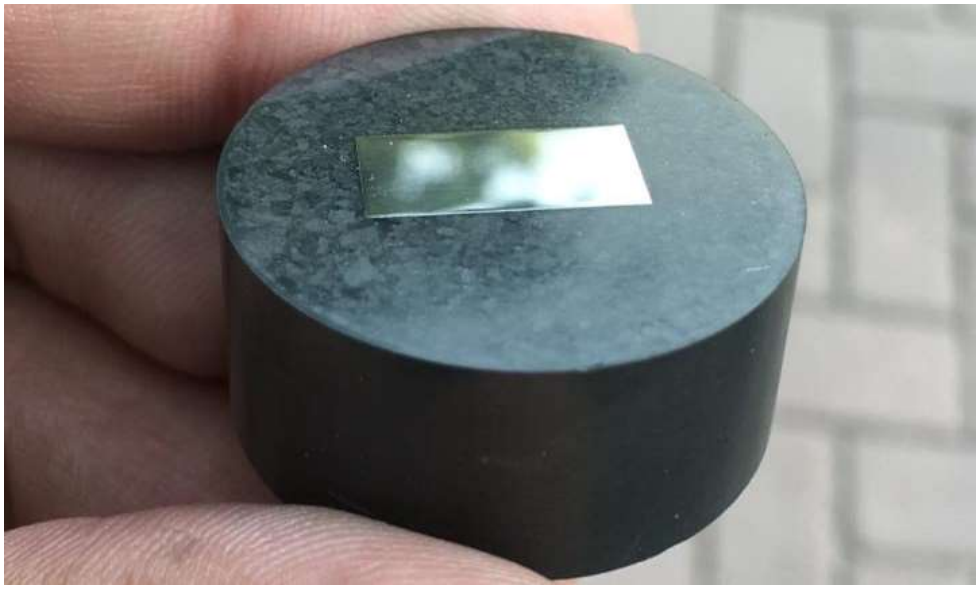

**Figure 21:** Mounted Polished Sample

Figure 21 shows the mounted material disc in which material is mounted inside the solid bakelite disc through Automatic Mounting Press. The shiny surface of the disc was due to the polishing of the mounted material which is discussed later in the methodology.

## 3.6 Grinding and Polishing

The grinding and polishing of the mounted material was done to refine the surface by reducing the surface roughness. These processes were performed to analyze the microstructure of the polished material and to analyze the laser re-melting details.

The automatic grinding and polishing machine was used for grinding and polishing purposes. It contained one movable head, two disc plates and a display. The movable head was controlled by an air compressor through display. The head contained piston and a rotatable plate with four slots for mounting material. The four pistons above the slots were used to apply the pressure individually on each mounted material disc.

The grinding and polishing papers were fixed manually on the circular rotatable lower disc plate. The display was to control the machine. The speed and rotation of head and plate, time of process, force applied and fluid jet were all controlled by the display.

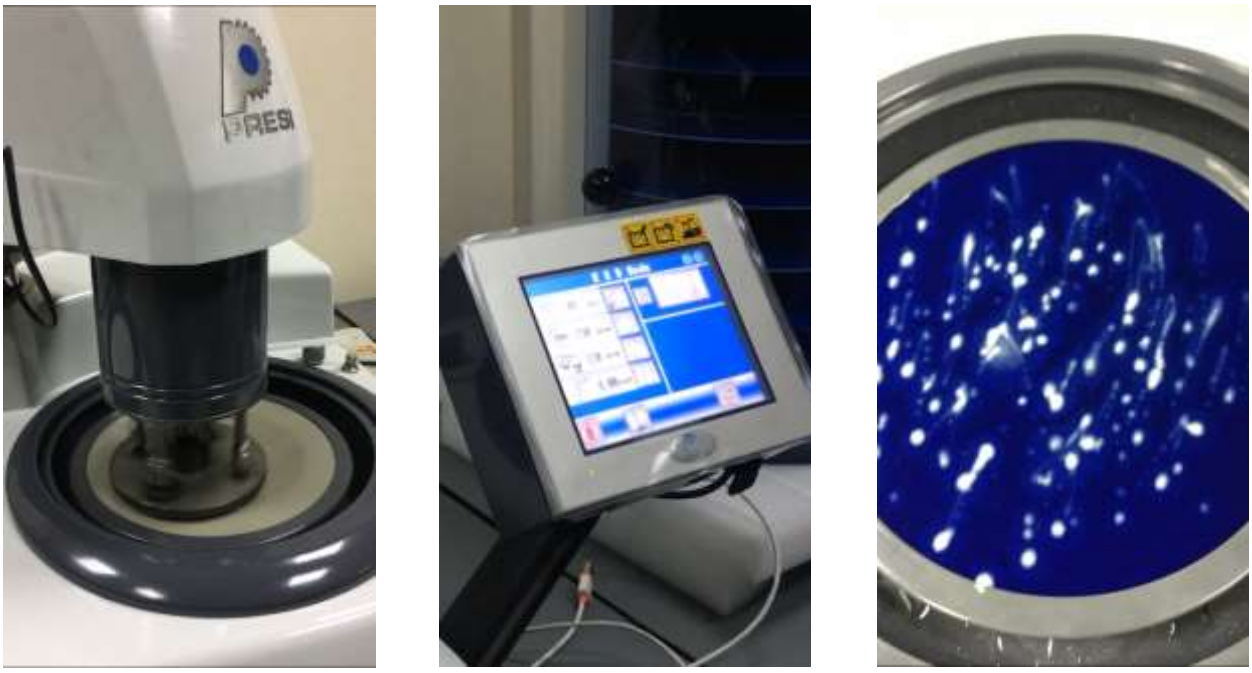


(a) (b) (c)

**Figure 22:** Automatic Grnding and Polishing Machine a) Grinding Process b) Display c)Polishing

Figure 22 shows the automatic grinding and Polishing Machine. The figure 22, part (a) shows the process of grinding, part (b) shows the display during grinding process and part (c) shows the polishing paper fixed on the rotating plate. The diamond suspension paste of 1µm roughness can be seen at the part (c) of the figure 22.

The FEPA P standard grinding papers were used from P800 to P4000 for grinding to reduce the surface roughness of the mounted samples. The grinding paper of P800 was used first as its grains were rough to remove the roughed surface of the EDM cut material. The grains became finer from P800 to P4000. The P4000 was the finest grinding paper used to fine the surface of mounted material.

The polishing process started with fixing a polishing paper on the plate and pouring a diamond suspension of 1µm roughness on the paper, then 0.5µm roughness Alumina solution on the same paper. The paper was then changed and polishing was performed at 0.1µm roughness Alumina Solution and at 50nm roughness Alumina Solution. The final surface roughness of the mounted material was 50nm after finishing the polishing process.

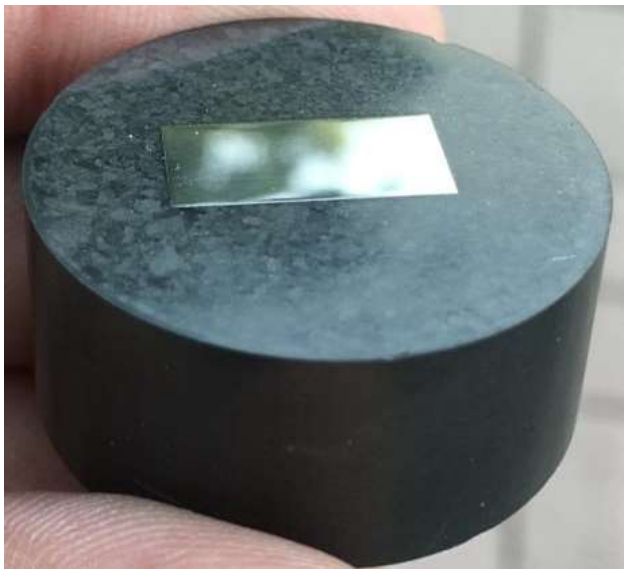

**Figure 23:** Polished Sample

Figure 23 shows the final polished sample. It was polished at 50nm surface roughness.

## 3.7 Etching [24]

The etching was a technique in metallography that was used to reveal the microstructure of a specimen under optical microscope. A polished specimen did not reveal its microstructure because the light was uniformly reflected in the optical microscope. The image contrast was produced by etching. Metallurgy contrasting methods included electrochemical, optical and physical etching techniques.

The chemical etching was used to reveal the microstructure of the samples. The most commonly used etchant for steels is Nital solution. The 2% Nital solution was prepared for etching.

**Figure 24:** Etched Surface of the Sample

The cotton was used to apply the etchant on each sample for 5-8 seconds. The shape of melt pool created by laser remelting became visible after the process of etching. Figure 24 shows the etched surface of the laser processed sample after applying 2% Nital etchant on its surface.

## 3.8 Optical Microscopy

It was an important tool to study the microstructure of the material. There was a limit on the size of a material that can be study depending upon the capacity of the microscope tray and its movement. The optical microscope had different magnifications to analyze the microstructure. The camera can be used on microscope to capture the images of the microstructure. It was also convenient to connect it to a computer to see the microscopic image on the computer display.

The polarized light microscope was used to analyze and take the images of the microstructure of the etched samples. The images were taken on different magnifications depending upon the study of the area. The polarized light optical microscope was used to have a better color combination than normal optical microscope. The most images taken were on the magnification of 200x or 50x including the magnification of the viewing lens.

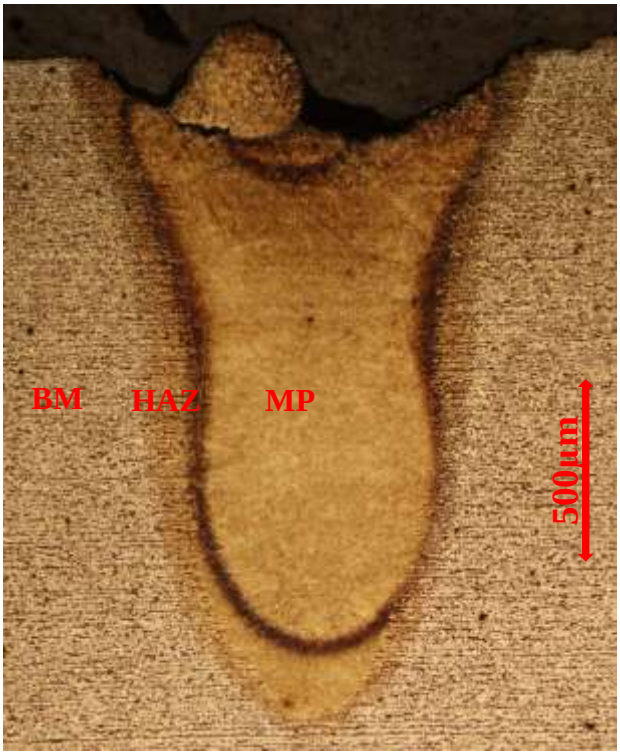


**Figure 25** Polarized Light Optical Microscope

Image at 50x

Figure 25 shows the polarized light optical microscopic image of a laser treated sample at 50x magnification. It shows the base material (BM), heat affected zone (HAZ), solidified melt pool (MP) and a scale for measurement. The microstructure was clear after etching for the study of laser treated sample. The magnification can also be increased to have a closer view of the sample depending about the lenses available for the microscope.

## 3.9 Nano-Hardness

The iMicro Nanoindenter of NANOMECHANICS, INC. has been used to analyze the nano hardness of the samples in three different areas; base material (BM), heat affected zone (HAZ) and melt pool (MP). It was capable of applying electromagnetic load of maximum 1000mN with a resolution of 6nN and less than 200nN of ultra low noise floors. It was capable of producing frequencies ranges from 0.1 Hz to 1 kHz. The sample movement of 100mm, 100mm and 25mm was achieved at the sample stage in x, y and z direction respectively [7].

The nano hardness machine was used to analyze the nano hardness of the sample in three different areas; base material (BM), heat affected zone (HAZ) and melt pool (MP). The laser remelting produced the changes in the microstructure as well as in the mechanical properties of the sample. The change in the hardness of the sample was analyzed through the nano hardness machine. The nano hardness machine was capable of performing a hardness test on a material with a maximum thickness of 10mm.

(a) (b)

**Figure 26:** Nano Hardness Machine a) Machine with Display b) Machine Mechanism

Figure 26 shows the images of Nano hardness machine in which part (a) shows outer image of the machine and part (b) shows the inside mechanism of the machine. The Nano hardness machine was connected to the computer to feed the input and also obtain the output.

The Nano hardness machine was used under the control load mode. The load was predetermined to be 100mN to avoid indenting only one phase of the microstructure of steel, which happened at the load of 10mN [26]. The Poisson's ratio was set to be 0.29 [27]. The indentations were programmed to be performed in a straight line starting from base material and ending in melt pool area.

The output was an optical microscopic image of 500x magnification of the indentations on the sample. It also displayed the data of load, depth of penetration, drift rate, average Nano hardness value and average elastic modulus value of each indent. The temperature and humidity was also mentioned in the output. The hardness trend in the different areas of the laser processed sample was analyzed later.

## 3.10 Micro Hardness

The WOLPERT Vickers micro hardness tester 402 MVD was used which integrated a sophisticated precision mechanism and a photoelectrical computer software system. It was designed to test the structure of tiny or minute metal parts, thin plates, metallic foil, high quality cord, thin hardening layers and electroplated layers. The indenter had pyramid shape with a face angle of 136˚ and the depth of the indentation was about 1/7 of its diagonal length [28].

The diamond pyramid shape micro indenter was used to apply the continuous predetermined force of 980mN or .98N onto the samples for 5 seconds. The micro hardness in Vickers scale (HV) was obtained by measuring the diagonals length of the indentation and inputting it into the integrated calculator. The size of the indent was important in measuring the hardness value.

The short sized indent gave the high value of hardness as the indenter was not able to penetrate deep into the material as compare to the large sized indent. The 400x magnification including the magnification of the viewing lens was used to measure the size of the indent which gave the value of hardness in HV scale.

**Figure 27:** Micro hardness tester 402 MVD

Figure 27 shows the Micro hardness tester 402 MVD which was used for obtaining the micro hardness values in HV scale. It was operated on control load mode in which load was predetermined and fed to the tester. The load ranges from 98mN to 9.8N. The load was controlled automatically. The Dwell time ranges from 5 to 99 sec. The tester was operated on HV test mode.

# CHAPTER 4: RESULTS AND DISCUSSION:

## 4.1 Effects of Laser Scans on the Surface of the Material (ED = 300 J/mm$^3$ and Different Defocuses):

Figure 28 shows five samples with laser scan having constant energy density of 300 J/mm$^3$

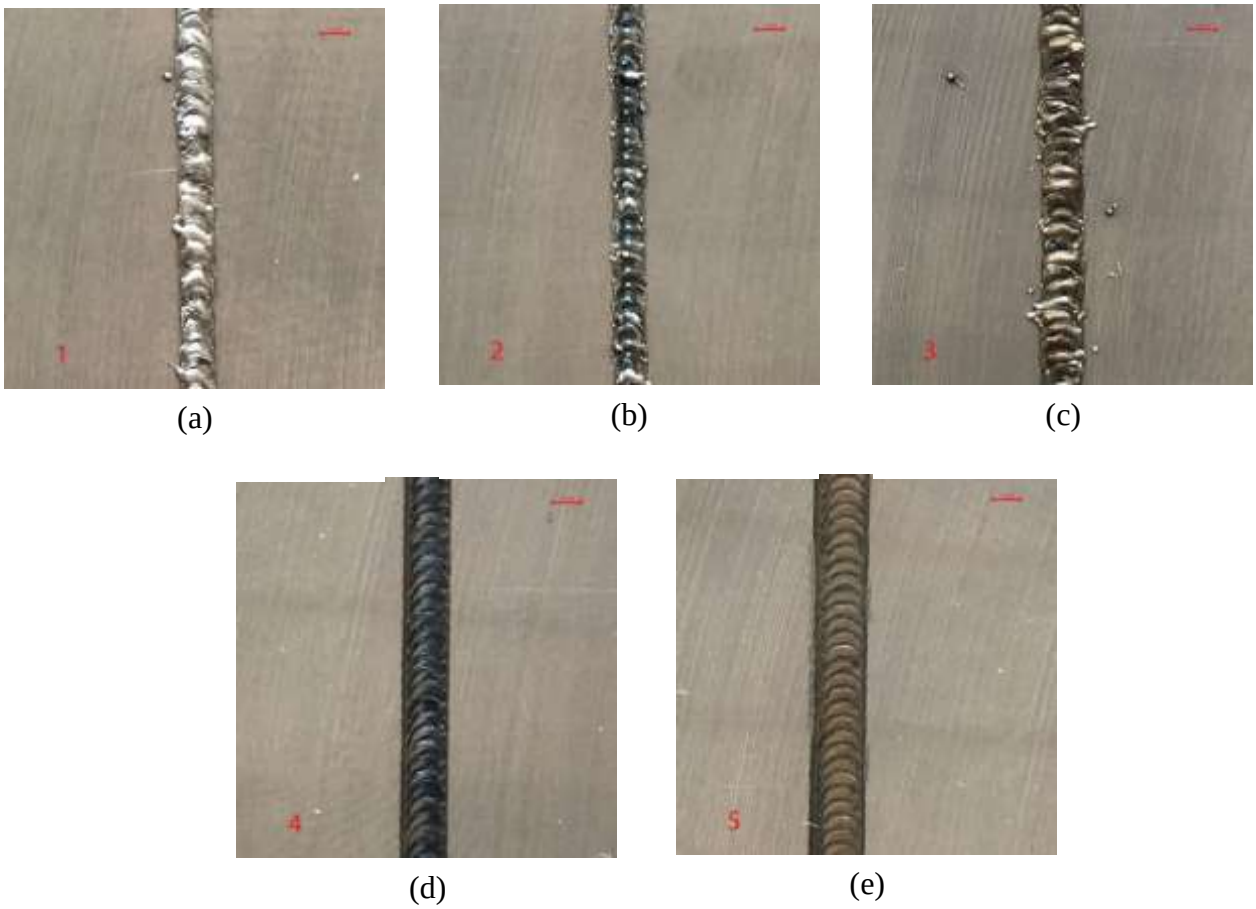


(a) (b) (c)

(d) (e)

**Figure 28:** The laser scan on steel samples having Energy Density of 300 J/mm$^3$ and; a) D.F = 0 mm, b) D.F = 2mm, c) D.F = 4mm, d) D.F = 8mm, e) D.F = 10mm

and different defocuses of the laser beam. The part (a) shows the surface of the sample at 0mm defocus, part (b) at 2mm defocus, part (c) at 4mm, part (d) at 8mm defocus and part (e) at 10mm of defocus. The different defocusing produced different shapes of the surface of the solidified material. The part (b) can be seen to have a lowest kerf width of all other laser scans and proved to be a focus point of a laser. The part (d) and (e) show the similar visual surface. The only difference that can be seen in the surfaces of part (d) and part (e) is of kerf width. The part (e) seems to have more kerf width than part (d). The kerf width increased as the defocus distance was increased from the focus point in both direction.

## 4.2 Effect of Defocusing of Laser Beam on Melt Pool Depth and Kerf Width at E.D = 300J/mm$^3$:

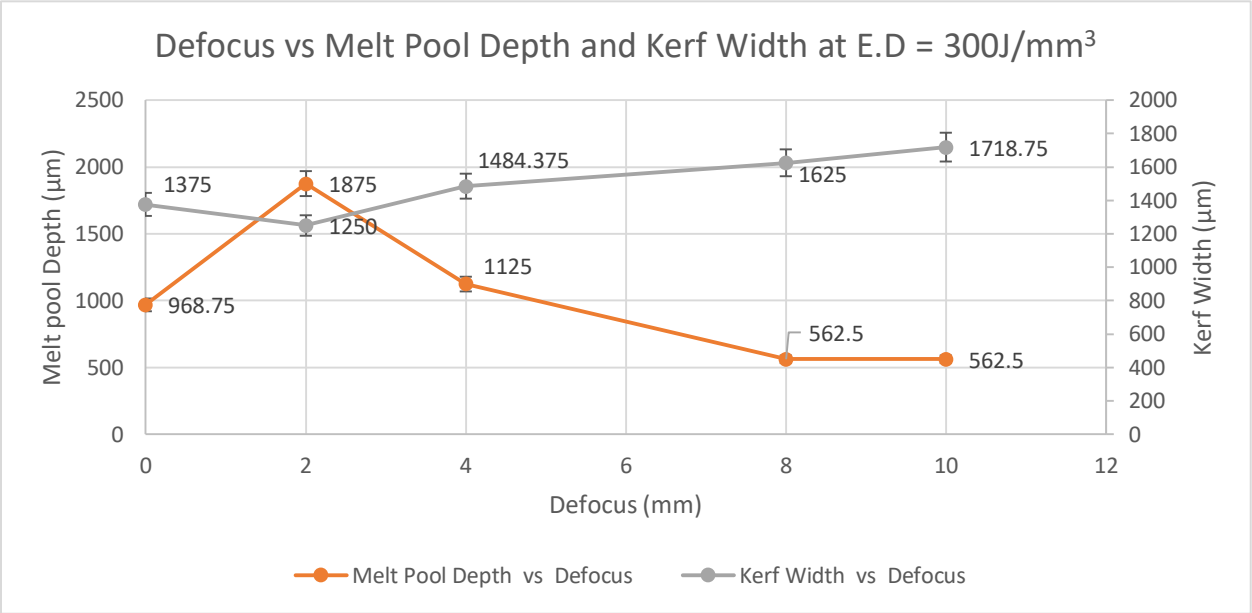


**Figure 29:** Melt pool depth and kerf width curves with defocusing of laser beam

Figure 29 shows the graph of five samples with different defocus of laser beam but same energy density. The graph is displayed as melt pool depth vs defocus and kerf width vs defocus. The x-axis represents defocus of a laser beam. The y-axis has two different axis; primary and secondary axis. The primary y-axis represents melt pool depth and is on the left side in the figure 29. The secondary y-axis represents kerf width and on the right side in the figure 30.

The figure 29 shows the defocusing effect of laser beam at constant laser energy density on melt pool depth and kerf width. The laser beam energy density was kept constant at 300 J/mm$^3$ by keeping spot size, scan speed and average power constant. The maximum melt pool depth and minimum kerf width was achieved at the focus point of the laser beam. The laser beam was focused at defocus of 2mm because it provided the maximum melt pool depth and minimum kerf width as compare to the other defocus points.

The melt pool depth decreased and kerf width increased as the laser beam defocusing distance increased on the both side of the focus point of 2mm. The another noticeable point in the figure 29 was that the melt pool depth became constant after certain value of defocusing which is 8mm in this case. The value of melt pool depth at defocus of 8mm and 10mm was the same.

## 4.3 Melt Pool Depth (E.D = 300J/mm$^3$ and Different Defocuses):

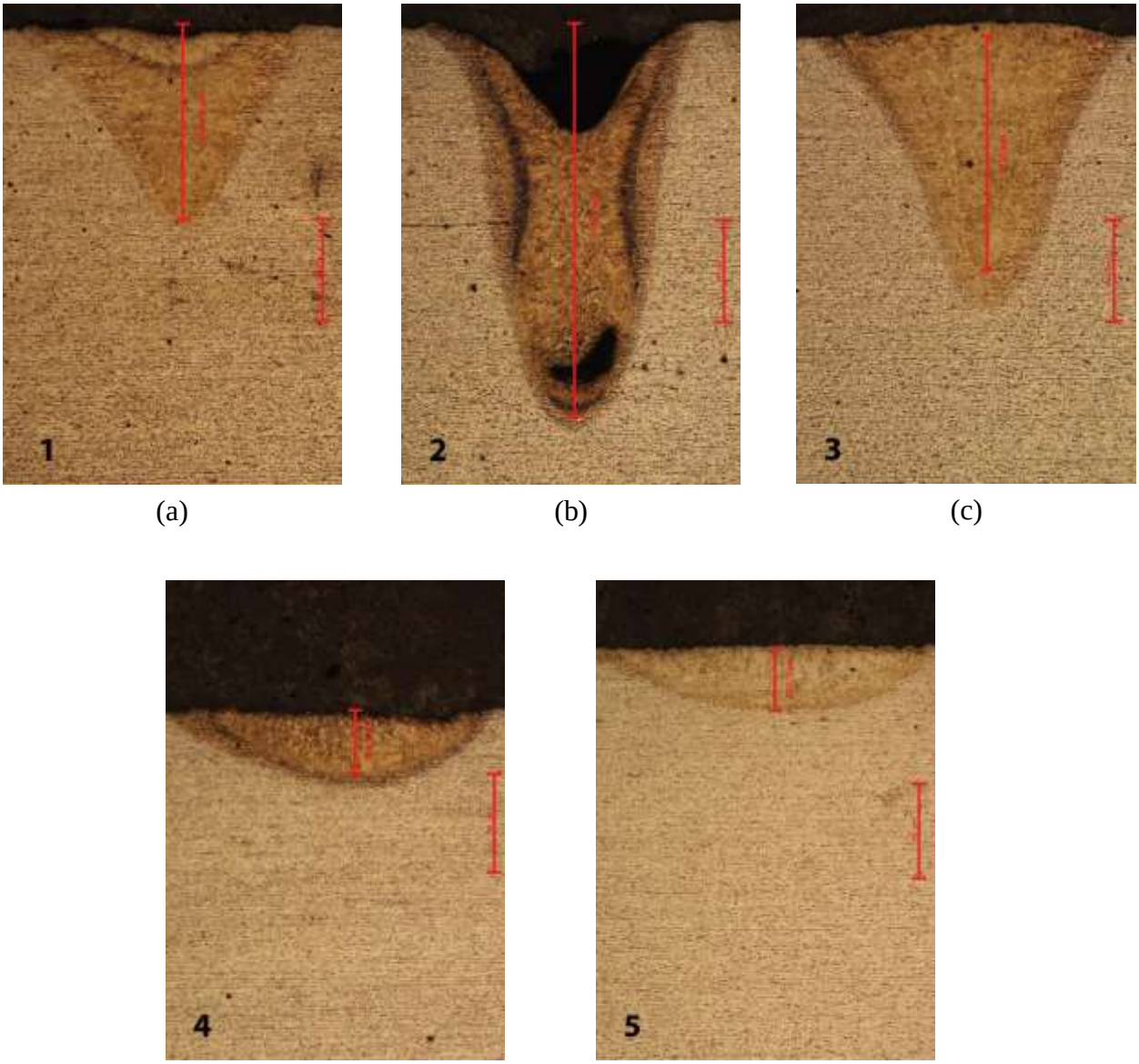


(a) (b) (c)

(d) (e)

**Figure 30:** Melt pool depth at defocus of a) 0mm b) 2mm c) 4mm d) 8mm e) 10mm

Figure 30 shows the melt pool depth of the five samples at different defocus but same energy density of the laser beam. The part (b) at defocus of 2mm gave the maximum depth of melt pool as compare to part (a), (c), (d) and part (e). It showed the focus point of the laser beam. The melt pool depth decreased as the laser defocus distance increased and became constant after the certain value of defocusing which is 8mm. The melt pool depth of part (d) and part (e) in the figure 30 was the same. The melt pool depth after certain defocus distance was observed to be constant.

## 4.4 Kerf Width (E.D = 300J/mm$^3$ and Different Defocuses):

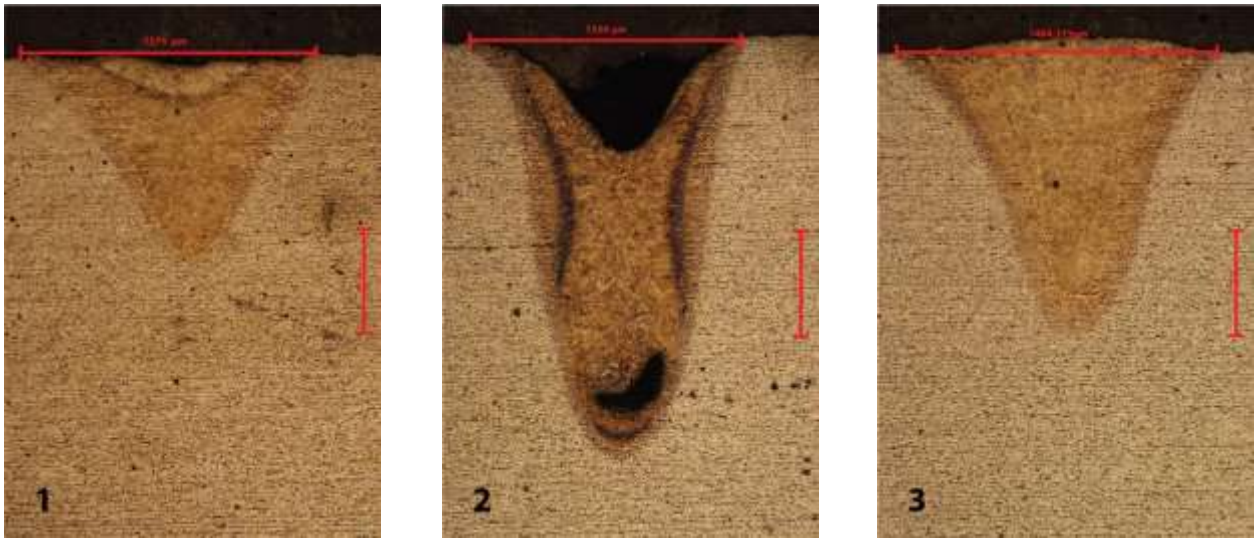


(a) (b) (c)

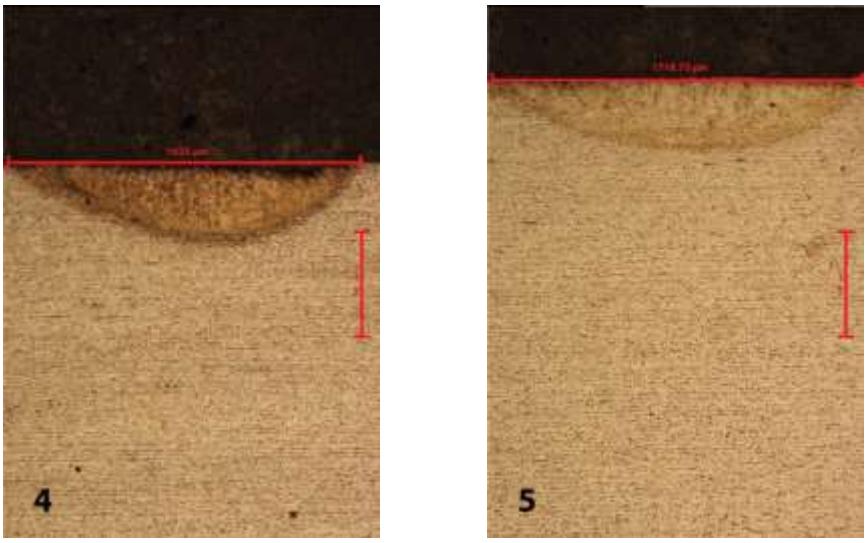


(d) (e)

**Figure 31:** Kerf Width at defocus of a) 0mm b) 2mm c) 4mm d) 8mm e) 10mm

Figure 31 shows the kerf width of the five samples under the condition of constant energy density of 300 J/mm$^3$ but different defocuses of laser beam. The minimum kerf can be seen in the part (b) as compare to the part (a), (c), (d) and part (e) which showed that the laser beam was focused at part (b). The variation of kerf width can be seen in the figure 31. The maximum kerf width can be seen in part (e). The difference of kerf width in part (d) and (e) can be observed low. The kerf width was expected to become constant after a certain value of defocus distance while keeping energy density constant.

## 4.5 Effects of Laser Scans on the Surface of a Material (Different ED but Constant Defocus of 2mm):

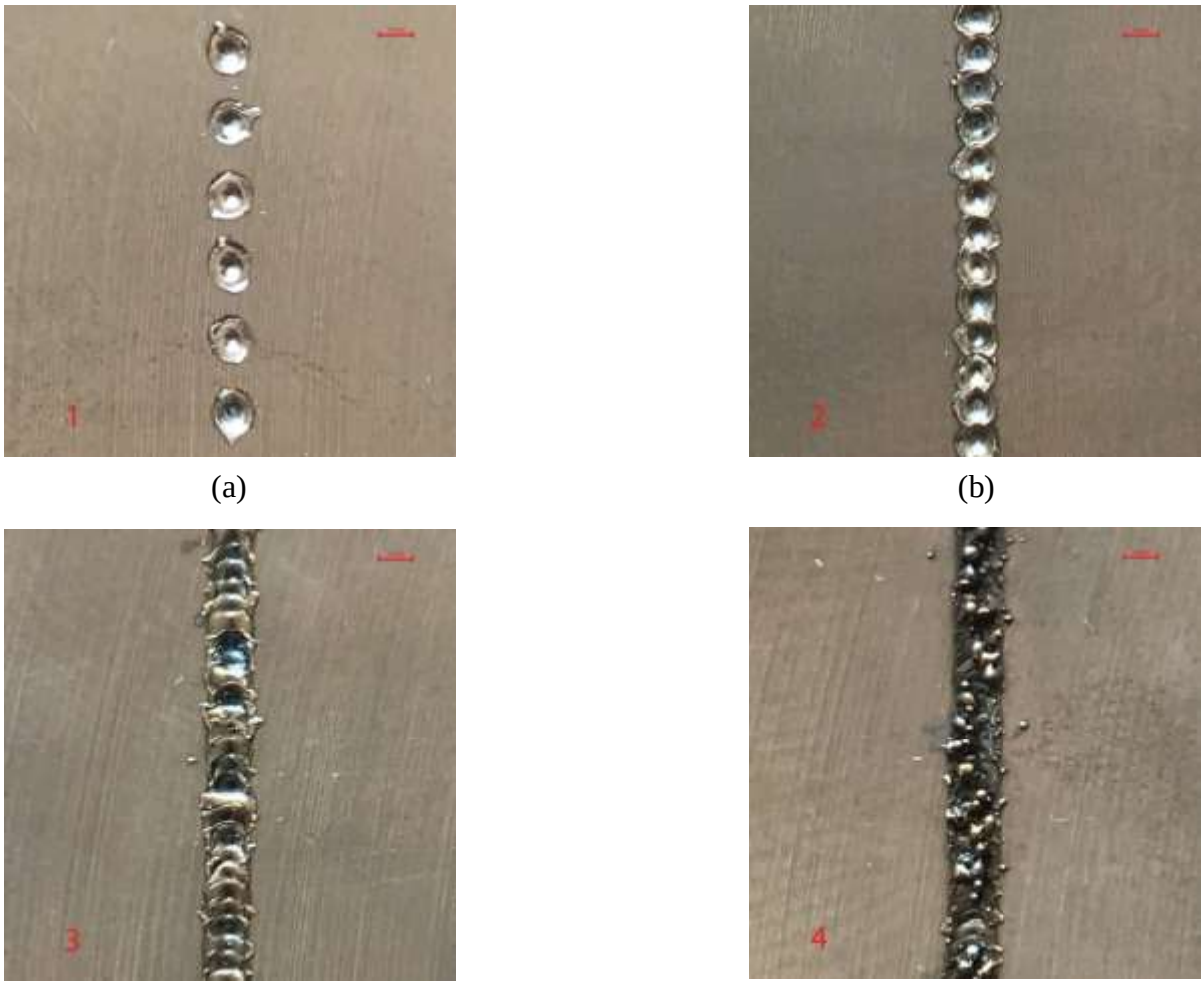


(a) (b)

(c) (d)

**Figure 32:** Laser scans on steel sample having defocus of 2mm and; a) E.D = 75 J/mm$^3$, b) E.D = 150 J/mm$^3$, c) E.D = 300 J/mm$^3$, d) E.D = 600 J/mm$^3$

Figure 32 shows four different laser scan surfaces having different scan speed and energy density. The gap between laser contact points on a material in part (a) of the figure 32 shows the high scan speed that the laser was unable to process the whole material. The gap was removed in part (b) by reducing the scan speed to fully process the material. The overlapping of contact points of laser in part (c) shows the further reduction in scan speed as compare to part (a) and part (b). The balling affect was produced in part (d), the laser scan below the balling affect is uniformly processed into the material. The decrease in scan speed increased the energy density. At higher energy densities, the laser beam had more time to penetrate into the material thus increasing the depth of penetration/melt pool and kerf width.

## 4.6 Effect of Energy Density on Melt Pool Depth and Kerf Width at Defocusing of 2mm:

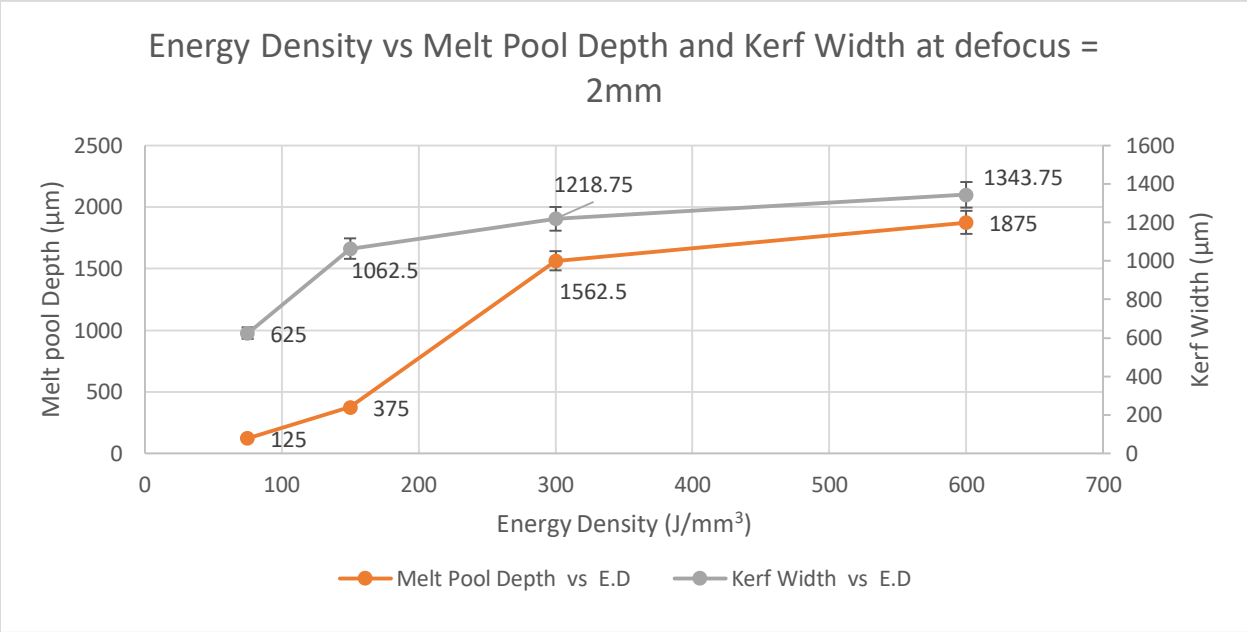


**Figure 33:** Melt pool depth and kerf width curves with varying energy densities

Figure 33 shows the graph of five samples with same defocus of 2mm but different energy densities of the laser beam. The graph is displayed as melt pool depth vs energy density and kerf width vs energy density. The x-axis represents energy density and four different energy densities were used to analyze their effect on melt pool depth and kerf width. The y-axis is divided into two axis; primary and secondary axis. The primary y-axis on the left in the figure 33 represents the melt pool depth and secondary y-axis on the right in the figure 33 represents the kerf width.

The graph in the figure 33 shows the energy density effect on the depth of penetration/melt pool depth and kerf width. The energy density was varied by changing scan speed while keeping the laser spot size and average power constant. The focused beam was used to get the maximum depth of penetration at different energy densities. The focus point was at 2mm defocus as described in the figure 29. The direct relationship can be seen of energy density with melt pool depth and kerf width.

The maximum depth of melt pool and kerf width was achieved at the maximum energy density. The depth of melt pool and kerf width can be increased by increasing the energy density of a focused laser beam. The melt pool depth and kerf width increased rapidly in the beginning as compare to the later part of the graph in the figure 33. It can be concluded that after certain energy density value, the increase in melt pool depth and kerf width was expected to be insignificant.

The sample 2 of the figure 29 and sample 3 of the figure 33 had same laser parameters as energy density of 300 J/mm$^3$ and defocus of 2mm but showed different melt pool depth and kerf width. The difference in melt pool depth of these samples occurred due to the porosity defect. It increased the melt pool depth in the sample 2 of the figure 29 as compare to the sample 3 of the

figure 33. The difference in the kerf width of both samples was in microns and considered to be insignificant.

## 4.7 Melt Pool Depth (D.F = 2mm and Different E.D):

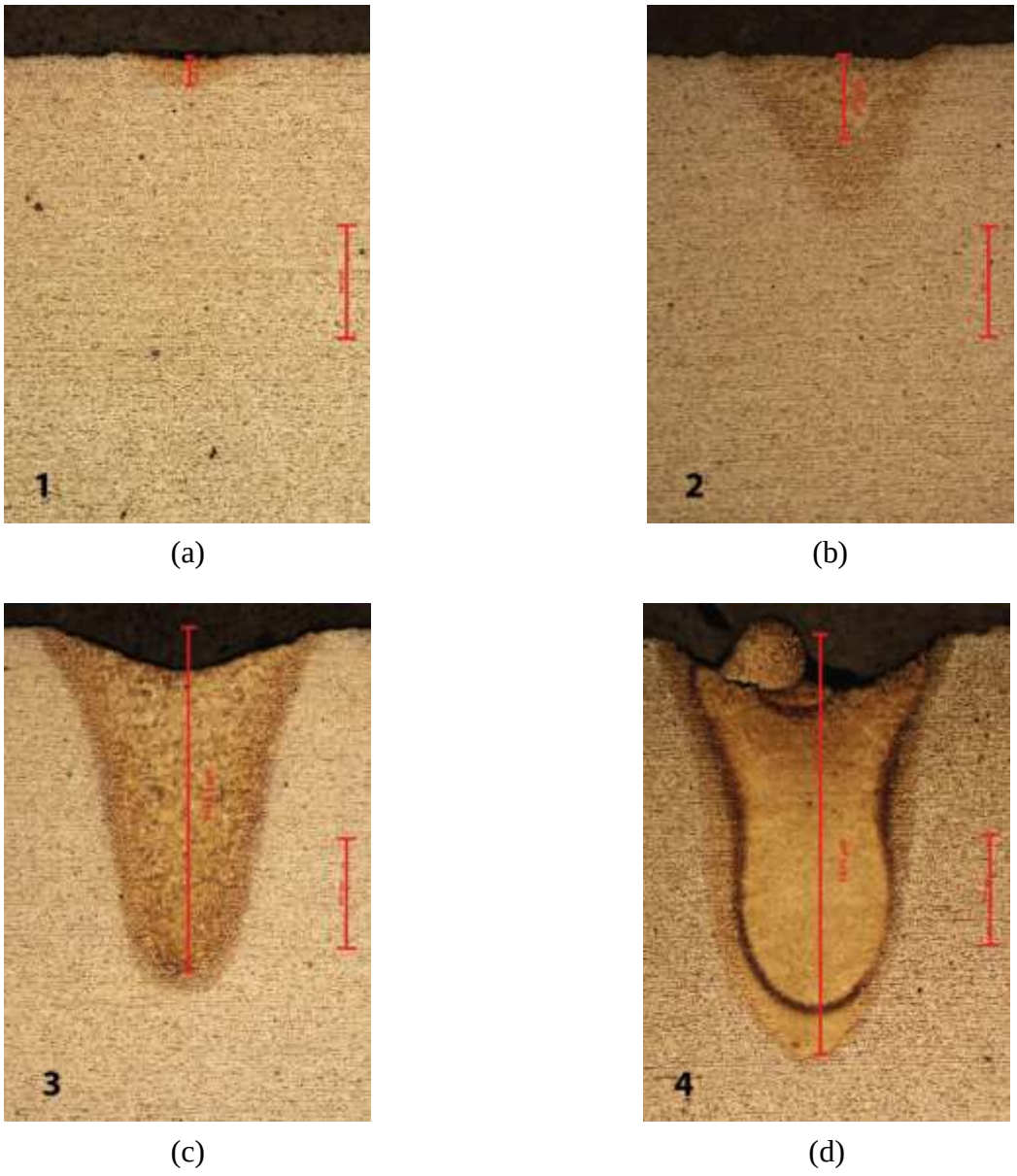


(a) (b)

(c) (d)

**Figure 34:** Melt pool depth at defocus of 2mm and energy density of a) 75 $J/mm^3$ b) 150 $J/mm^3$ c) 300 $J/mm^3$ d) 600 $J/mm^3$

Figure 34 shows the melt pool depth of laser treated samples with different energy densities but constant defocus of 2mm. The direct relation can be seen of energy density with melt pool depth. The increase in energy density resulted in increase of melt pool depth. The maximum melt pool depth can be seen in part (d) when energy density was kept at 600 $J/mm^3$ and minimum depth was observed at the energy density of 75 $J/mm^3$.

## 4.8 Kerf Width (D.F = 2mm and Different E.D):

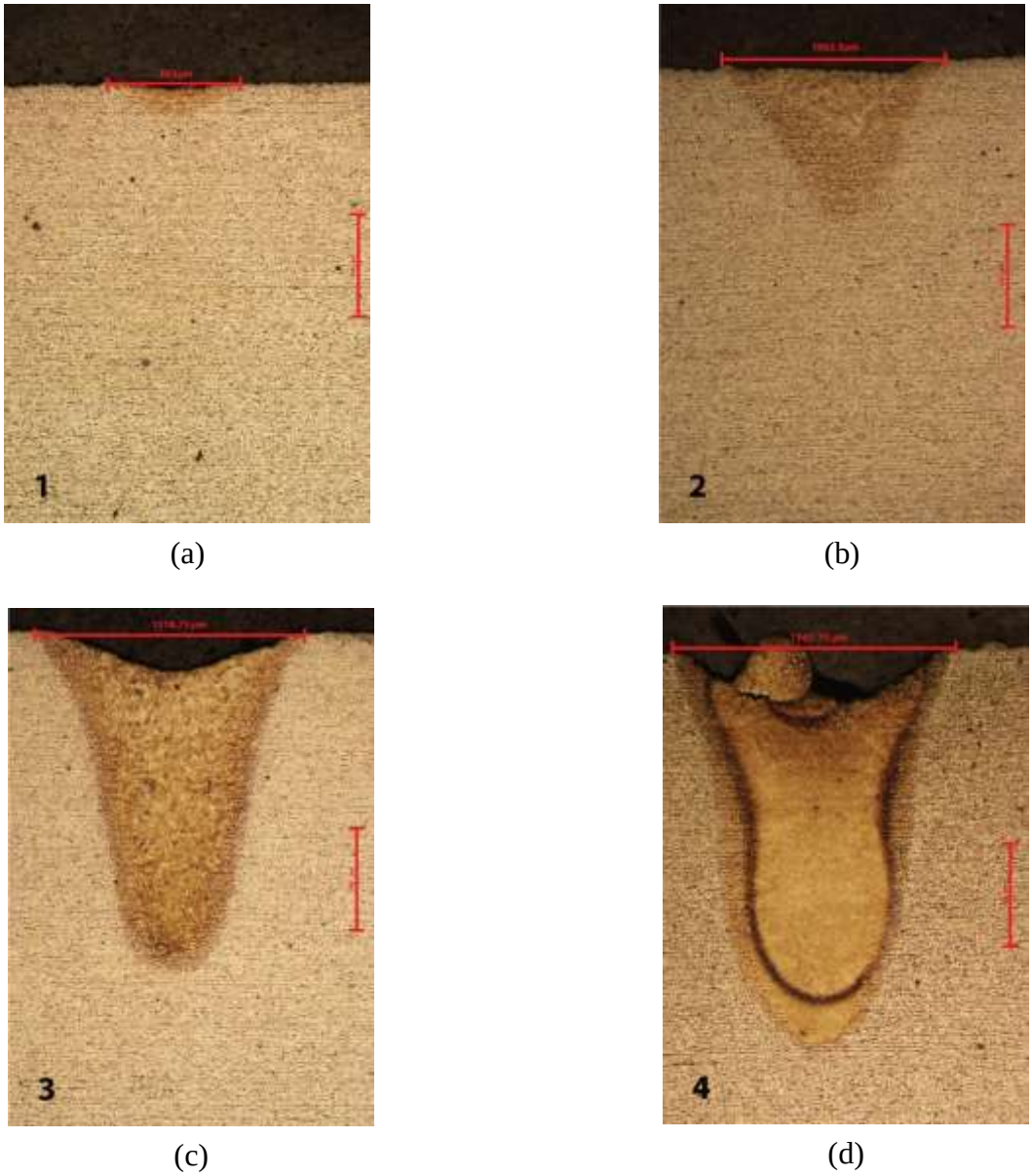


(a) (b)

(c) (d)

**Figure 35:** Kerf width at defocus of 2mm and energy density of a) 75 J/mm$^3$ b) 150 J/mm$^3$ c) 300 J/mm$^3$ d) 600 J/mm$^3$

Figure 35 shows the kerf width of the samples at constant defocus of 2mm but different energy densities. The minimum kerf width can be seen in part (a), when energy density was low. The maximum kerf width cab be observed at the maximum energy density. The linear relationship can be seen between energy densities with kerf width in the figure 33. The difference in kerf width of part (a) and part (b) was high as compare to the difference of part (b) and part (c) or part (c) and part (d). The difference of kerf width in part (c) and part (d) was low. The energy densities were observed to have a considerable effect on kerf width up to a limit, after which the effect was not expected to be prominent.

## 4.9 Micro hardness vs Nano hardness:

## 4.10 Graph with ED = 300 J/mm$^3$ but different defocus:

### 4.10.1 Sample 1 (DF = 0mm, ED = 300 J/mm$^3$):

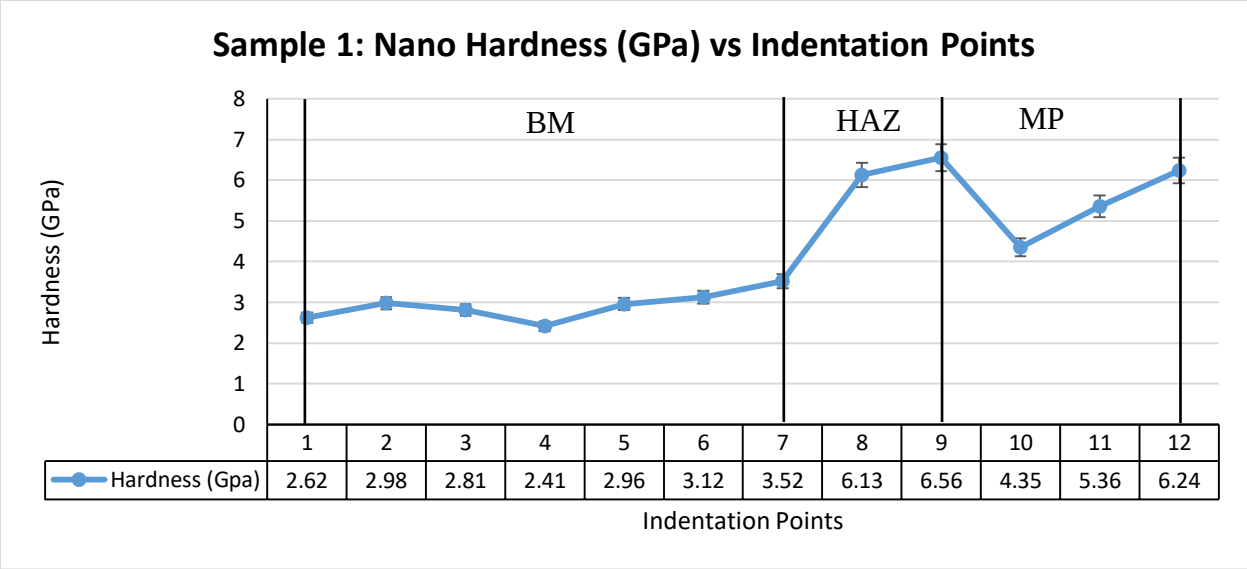


**Figure 36:** Nano hardness of laser treated sample having ED = 300 J/mm$^3$ and defocus of 0mm

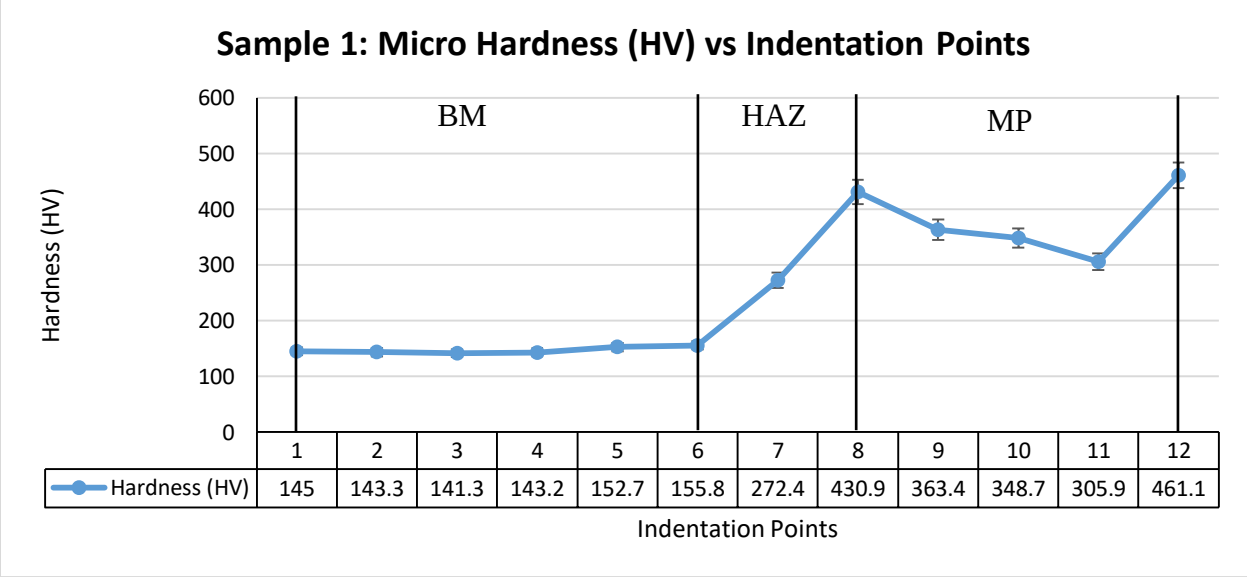


**Figure 37:** Micro hardness of laser treated sample having ED - 300 J/mm$^3$ and defocus of 0mm

Figure 36 shows a graph between nano hardness and indentation points. The y-axis shows the nano hardness in GPa and x-axis shows the number of indentation points. The graph was divided into three areas; BM, HAZ and MP. The nano-indenter was programmed to take 12 indents in such a way that first indent was taken in BM and the last indent inside MP. The first 7 indentation points of nano-hardness lied in BM, next 2 points in HAZ and last 3 points in MP.

Figure 37 is similar to the figure 36 except it has micro hardness (HV) instead of nano-hardness on y-axis. The starting position of the micro hardness indenter was different from the nano-hardness indenter. That was the reason that the three areas in the figure 37 were shifted to a slight left as compare to the areas in the figure 36. The first 6 micro hardness indentation points lied in BM, next 2 points in HAZ and last 4 points in MP.

The overall trend of the hardness in figure 36 and figure 37 was the same. The change in the hardness of the BM area was very small and was considered insignificant. The hardness value increased significantly inside HAZ area. The maximum hardness can be observed at the interface of HAZ and MP. The MP had high hardness near its interface with HAZ because of the high cooling rate. The MP near its interface with HAZ had interaction with the solid phase thus increased the cooling rates near its interface. The center of the MP had the low value of hardness. It was because of the slow cooling at the center of the MP. The trend of hardness can be observed to be similar in solidification process of welded material [12].

#### 4.10.1.1 Optical Microscopy:

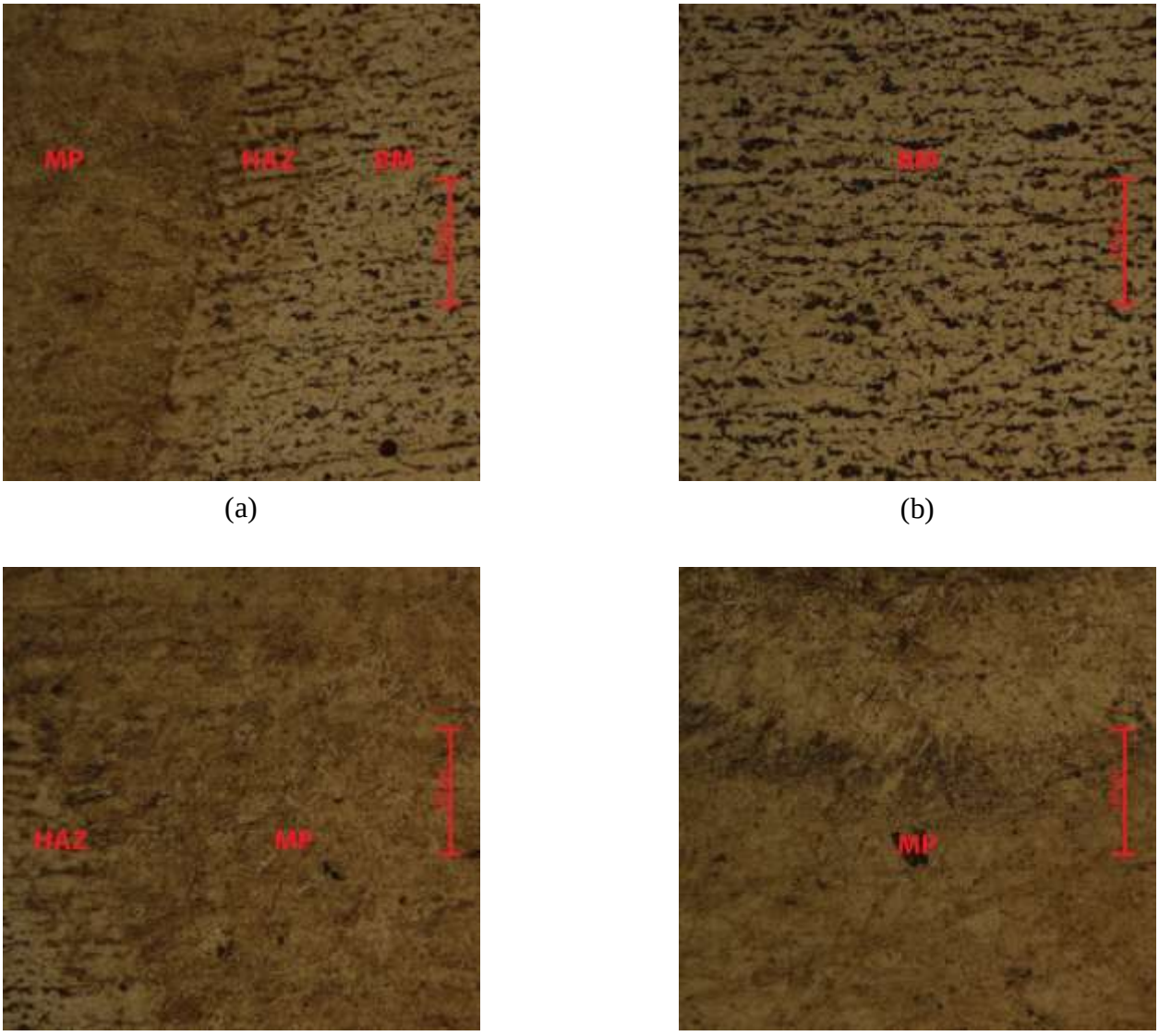


(a) (b)

(c) (d)

**Figure 38:** Microstructure of Laser treated Sample a) BM, HAZ, MP b) BM c) HAZ, MP d)MP

The figure 38 shows the micro-structure of the laser treated sample having ED of 300 J/mm$^3$ and defocus of 0 mm. The figure 38, part (a) shows the microstructure of BM, HAZ and MP, part (b) shows the microstructure of BM which consisted of ferrite pearlite microstructure, further more pearlite was a mixture of two phases; ferrite and cementite [29], part (c) shows the microstructure of HAZ which was the same as of BM except have smaller grain size and part (d) shows the microstructure of MP which was the combination of martensite, bainite and fine pearlite [29].

The BM microstructure had larger grain size as compare to the grain size in HAZ area and can be visualized in the figure 38, part (a). The larger grains showed low toughness and smaller

grains showed high toughness [13], which implies HAZ had more toughness as compare to the BM. The microstructure of MP was a combination of martensite, bainite and fine pearlite ferrite microstructure depending upon the cooling rate [29]. The fast cooling rate from austenite resulted in the formation of martensite in steels and cooling rate slower than that for martensite formation and faster than that for fine pearlite ferrite formation resulted in the formation of bainite microstructure [14].

The fine pearlite ferrite microstructure was a grain refinement process which was expected to increase the toughness of the steel [30]. The formation of high angled boundaries bainite packet [16] in the microstructure led to good toughness. The refinement of the austenite grain size and rapid cooling rate decreased the formed martensite packets size which was expected to improve the toughness of the sample [15].

Fracture toughness was an essential property of a material, indicating the strain energy absorbing ability of a material prior to fracture. The higher fracture toughness showed the higher resistance of material towards crack propagation. This resistance increased the stress cycles to failure of a material. In other words, it prevented the crack propagation and increased fatigue life of a material [19].

### 4.10.2 Sample 2 (DF = 2mm, ED = 300 J/mm$^3$):

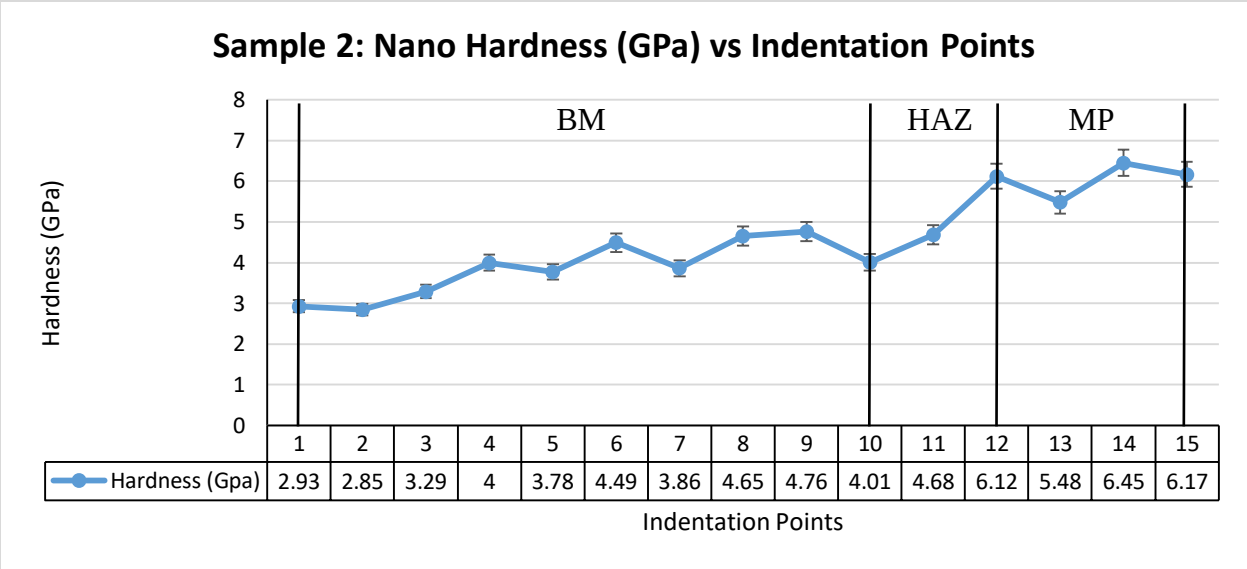


**Figure 39:** Nano Hardness of laser treated sample having Ed - 300 J/mm$^3$ and defocus of 2mm

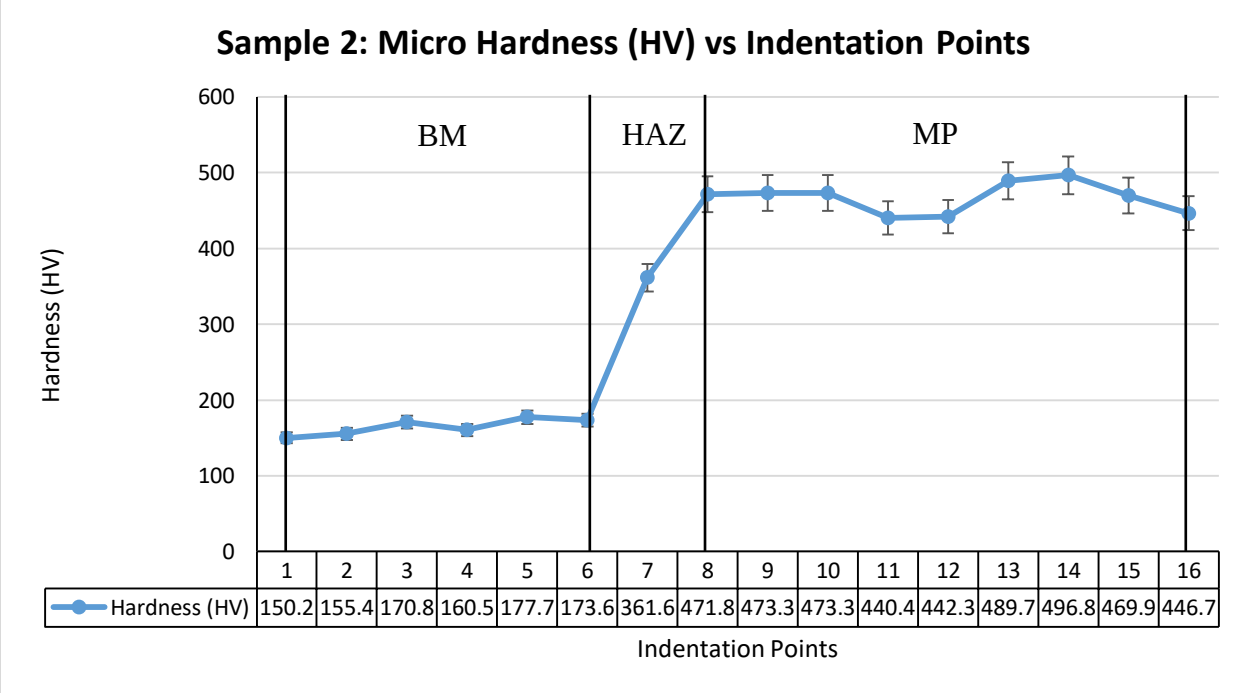


**Figure 40:** Micro Hardness of Laser treated sample having ED = 300 J/mm$^3$ and defocus of 2mm

Figure 39 is similar to the figure 36 except the indentation points taken were total of 15 points. The indenter initial position was fixed in such a way that the first 10 points lied in BM, next 2 in HAZ and last 3 in MP.

Figure 40 is similar to figure 37 except total points of indentations were 16 in the figure 40. The starting of position of the micro hardness indenter in the figure 40 was different as compare to the starting position of nano hardness indenter in the figure 39. The difference between both figures was total number of indentation points and their distribution in three areas of the processed material i.e. BM, HAZ and MP. The first 6 points lied in BM, next 2 in HAZ and last 8 in the MP. The three areas in the figure 40 were shifted towards left as compare to the areas position in the figure 39 because of the different starting position of the measurements.

The overall trend of the hardness in figure 39 and figure 40 was same as the hardness in the BM was considered constant due to the low variation in hardness values, the abrupt increase in hardness was observed as the indentations were taken in HAZ. The hardness values were high in MP near the interface of the HAZ and MP as compare to the hardness values at the center of the MP. The maximum hardness can be observed at the interface of HAZ and MP. The high values of hardness in MP near its interface with HAZ was because of the rapid cooling rate and it was due to its interaction with the solid phase. The low cooling rates at the center of the MP gave low values of hardness. The solidification process agreed with the curves of both figures mentioned above [12].

#### 4.10.2.1 Optical Microscopy:

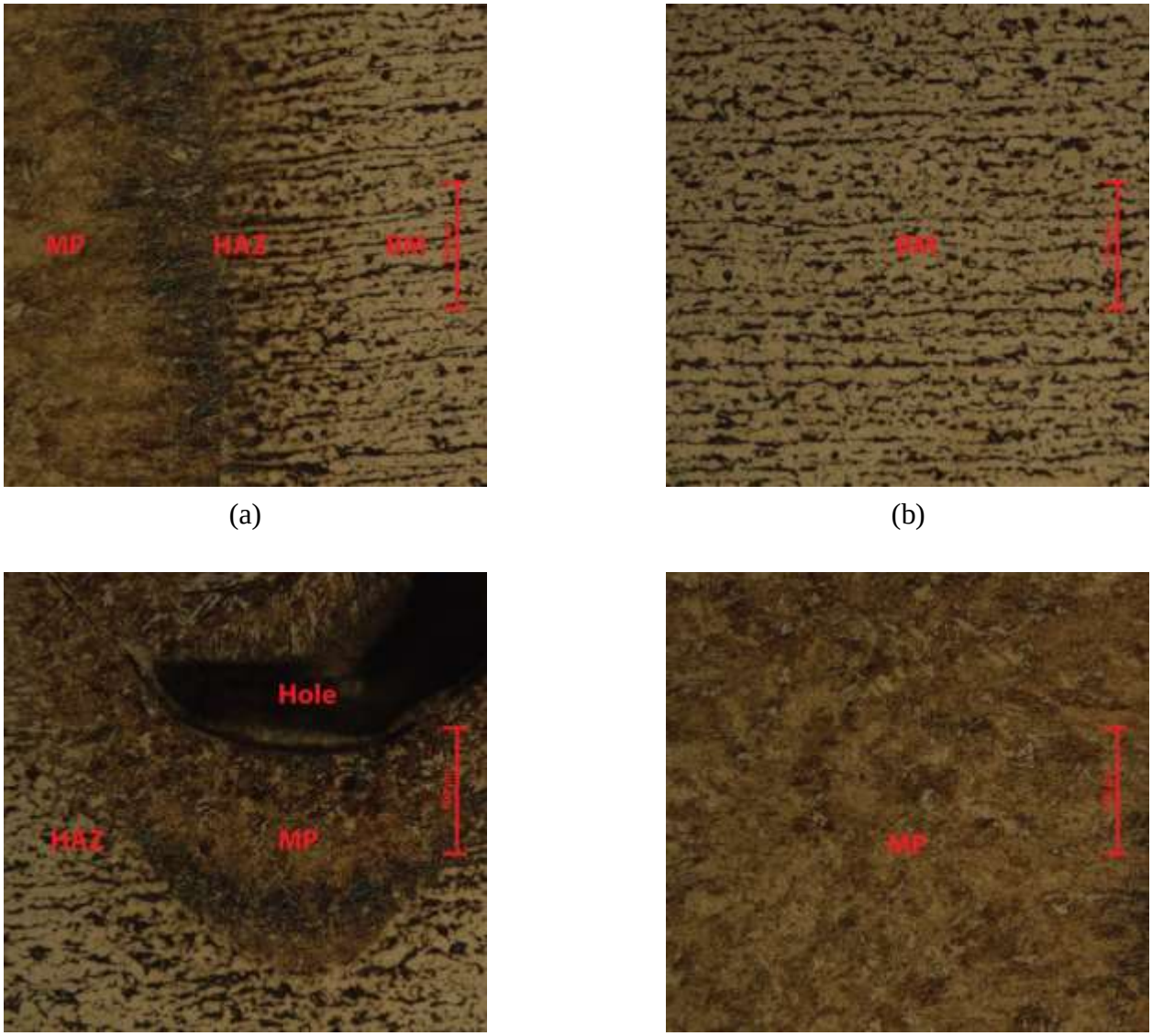


**Figure 41:** Microstructure of Laser treated sample a) BM, HAZ, MP b) BM c)HAZ, MP, Hole d)MP

Figure 41 is similar to the figure 38. It shows the microstructure of laser treated sample having ED of 300 J/mm$^3$ and defocus of 2mm. The part (a) shows the BM, HAZ and MP, part (b) shows the BM, part (c) shows the HAZ, MP and porosity defect and part (d) shows the MP. The microstructure of BM, HAZ and MP in the figure 41 was similar to that of the figure 38. The percentage of martensite, bainite and fine pearlite ferrite in the MP of the figure 41 was expected to be different than that of the figure 38. The toughness in the MP and HAZ of this sample was expected to increase similar to the figure 38. The crack resistance was also expected to increase due to improved toughness of laser treated area.

**Sample 3 (DF = 4mm, ED = 300 J/mm$^3$):**

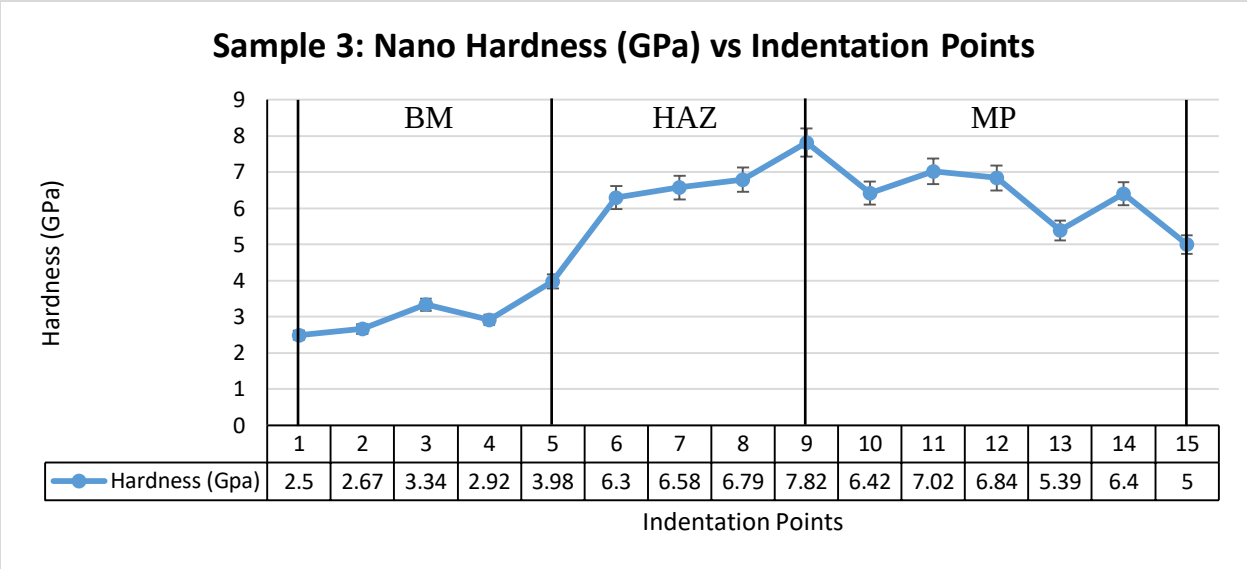


**Figure 42:** Nano Hardness of laser treated sample having ED = 300 J/mm$^3$ and defocus of 4mm

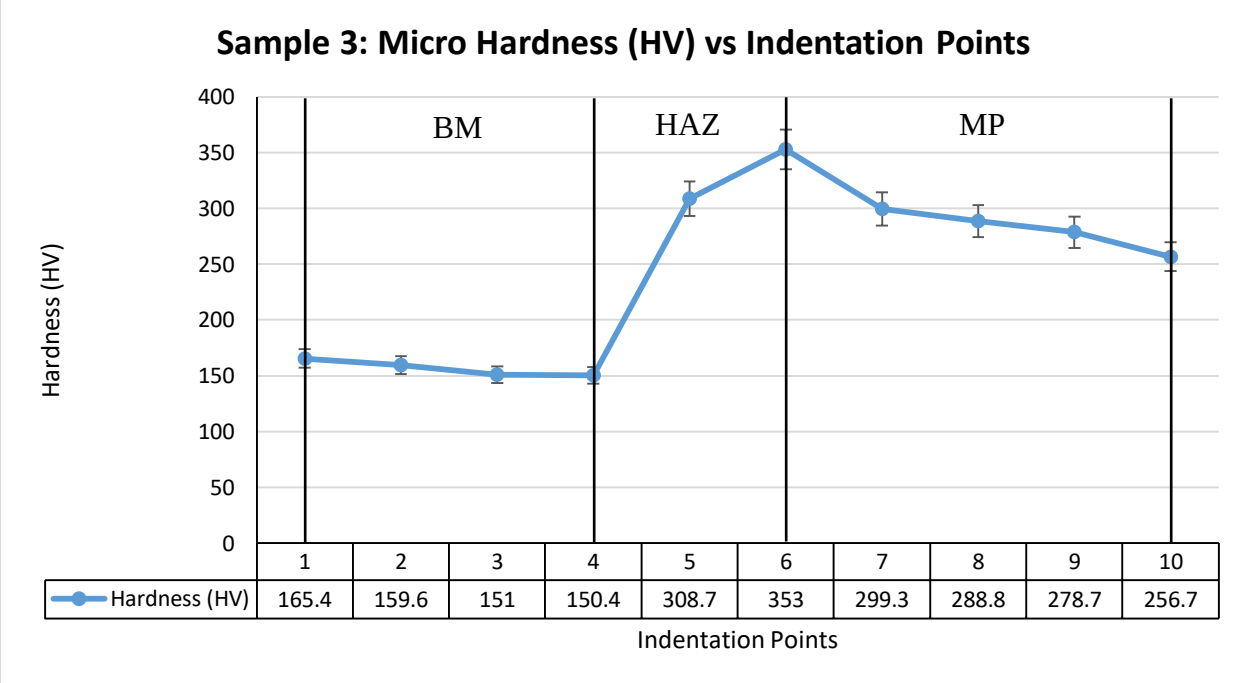


**Figure 43:** Micro hardness of laser treated sample having ED = 300 J/mm$^3$ and defocus of 4mm

Figure 42 is similar to the figure 36 except the total indentation points taken in the figure 42 is 15. The first 5 points were taken in BM, next 4 in HAZ and last 6 inside MP.

Figure 43 is similar to the figure 37 except the total indentation points were 10 in the figure 43. The starting position of micro indenter was different as compare to the starting position of nano indenter in the figure 42. The size of the micro indenter was big as compare to the size of the nano

indenter. It increased the number of indentation points taken in HAZ by nano hardness indenter as compare to the points in HAZ by micro hardness indenter.

The overall hardness trend in the figure 42 and 43 was the same. The BM showed the constant value of hardness considering low fluctuation insignificant. The hardness increased in the HAZ abruptly and had the maximum value at the interface of the HAZ and MP. The MP area near to its interface with HAZ showed high hardness because of the rapid cooling rate at that area which was due to its interaction with solid phase. The center of the MP had low hardness because of the low cooling rate. The overall hardness trend in solidification process followed the same hardness trend as mentioned in the figure 42 and 43 above [12].

#### 4.10.2.2 Optical Microscopy:

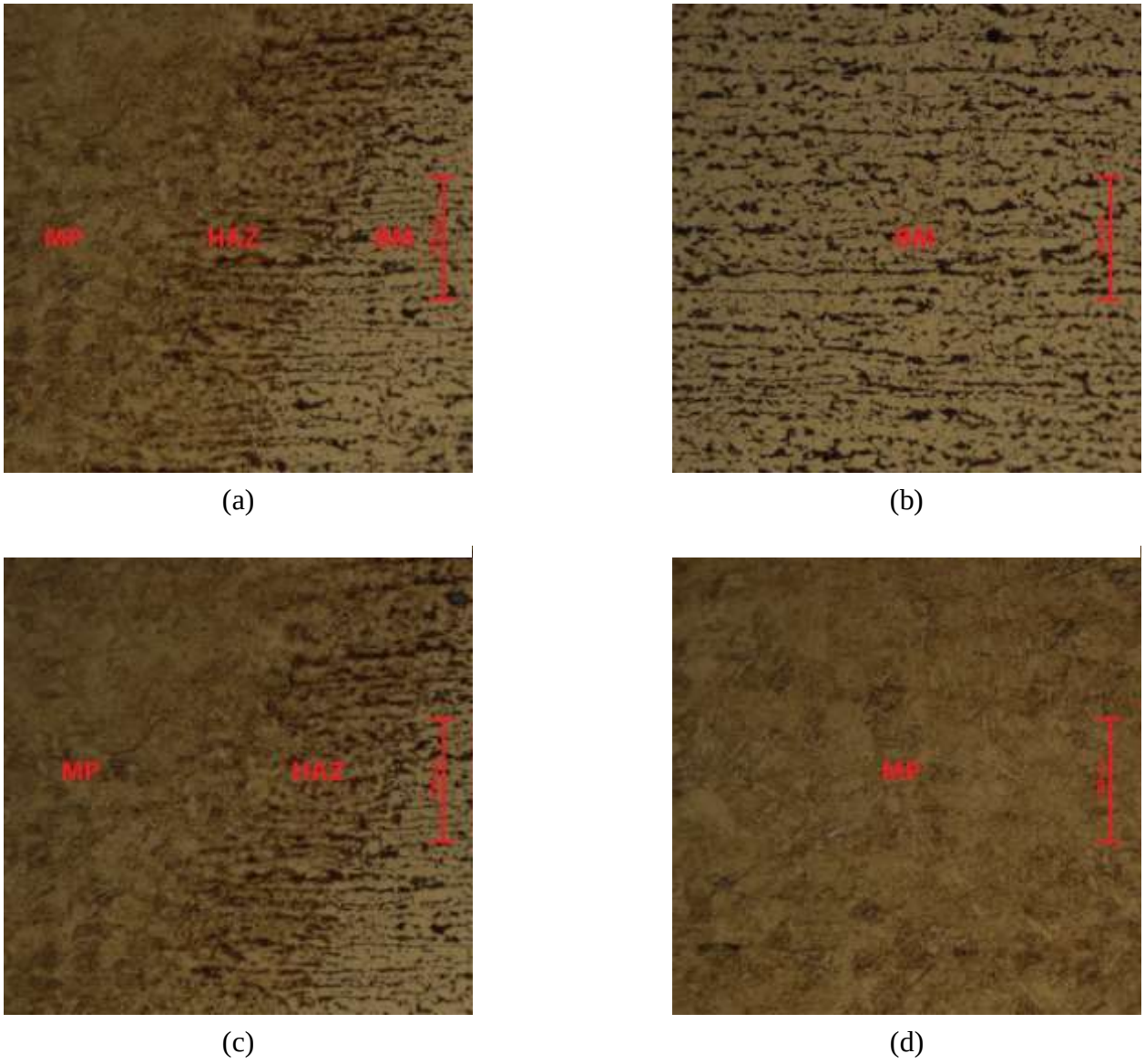


(a) (b)

(c) (d)

**Figure 44:** Microstructure of laser treated sample a) BM, HAZ & MP b) BM c) HAZ & MP d) MP

Figure 44 represents the microstructure of laser treated sample having ED of 300 J/mm$^3$ and defocus of 4mm. It is similar to the figure 38 except the percentage of martensite, bainite and fine pearlite ferrite microstructure In MP was different as that of the figure 44, part (d). The toughness of the MP in the figure 44 was expected to increase due to the grain refinement in MP similar to that of the figure 38. The increased toughness results in better fatigue resistance or fatigue life which was expected to prevent the crack from propagation.

### 4.10.3 Sample 4 (DF = 8mm, ED = 300 J/mm$^3$):

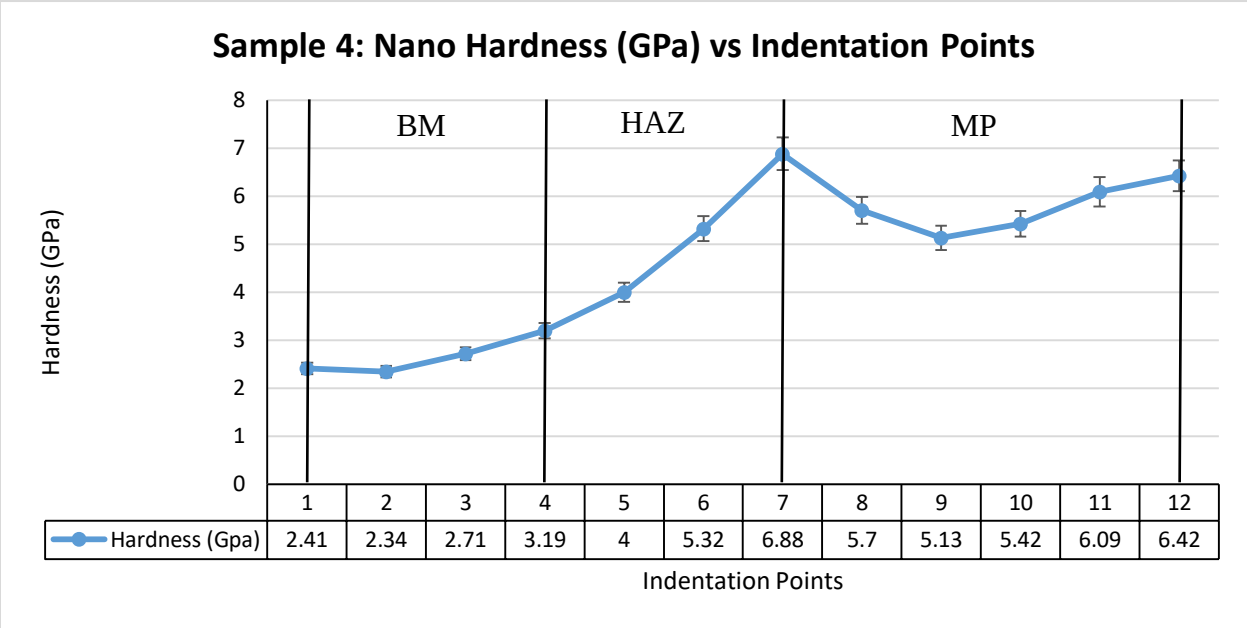


**Figure 45:** Nano hardness of laser treated sample having ED = 300 J/mm$^3$ and defocus of 8mm

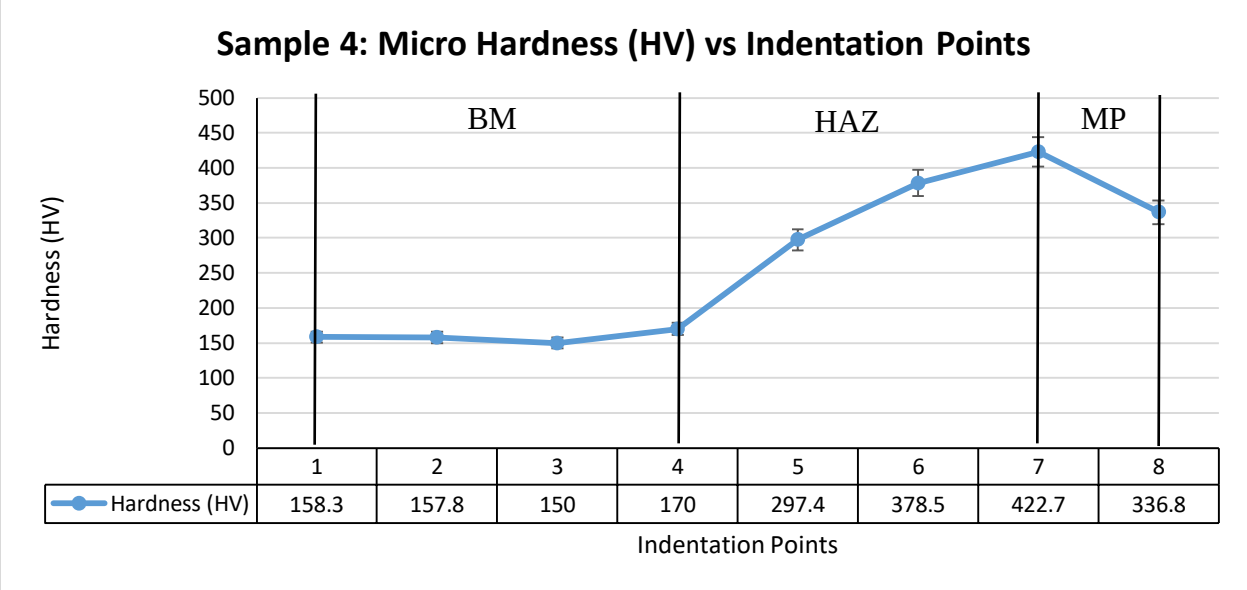


**Figure 46:** Micro hardness of laser treated sample having ED = 300 J/mm3 and defocus of 8mm

Figure 45 is similar to the figure 36. The difference between both figures was between the distributions of indentation points into three areas; BM, HAZ and MP. The first 4 point lied in the BM, next 3 in HAZ and last 5 in MP.

Figure 46 is similar to the figure 37 except the total indentation points taken in the figure 46 was 8. The first 4 points lied in BM, next 3 in HAZ and last 1 in MP.

The overall trend of hardness in the figure 45 and 46 were the same. The hardness value in BM was considered constant due to insignificant fluctuations in hardness values in BM. The hardness value changed significantly in HAZ area and the maximum value of hardness was observed at the interface of the HAZ and MP. The indentation points in MP which were near the interface of MP and HAZ showed high hardness value because of the rapid cooling due to its interaction with solid phase. The center of MP had low hardness value due to slow cooling. The overall trend of hardness followed the solidification process hardness trend [12].

#### 4.10.3.1 Optical Microscopy:

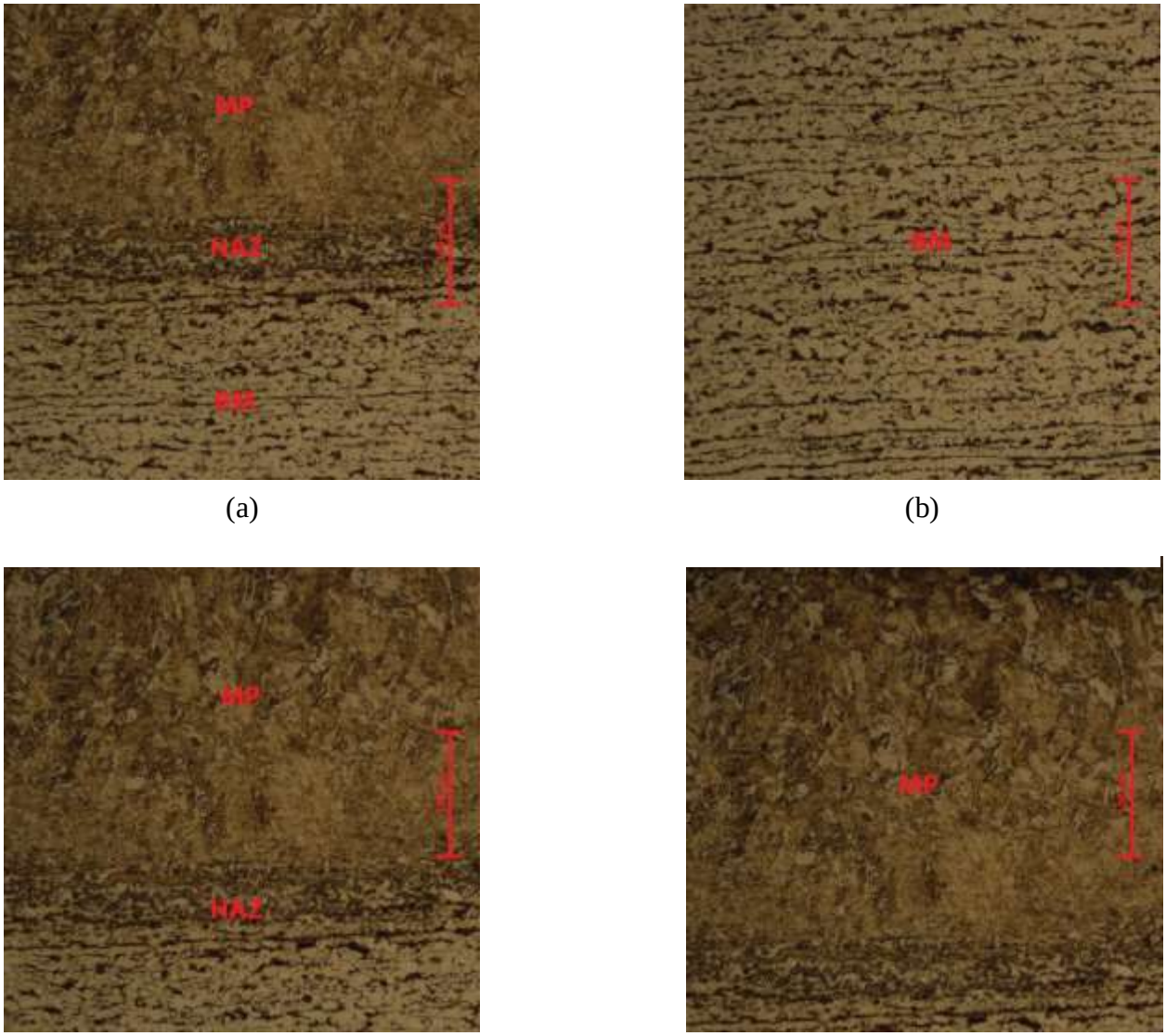


(a) (b)

(c) (d)

**Figure 47:** Microstructure of laser treated sample a) BM, HAZ & MP b) BM c) HAZ & MP d) MP

Figure 47 represents the microstructure of laser treated sample having ED of 300 J/mm$^3$ and defocus of 8mm. It is similar to the figure 38 except the percentage of martensite, bainite and fine pearlite ferrite microstructure in MP was different. This can be visualized in the figure 47. The toughness has increased as the grain was refined in the MP area similar to that of the figure 38. The higher the toughness, the higher the material was expected to resist the crack propagation. This was expected to improve the fatigue life of the sample.

### 4.10.4 Sample 5 (DF = 10mm, ED = 300 J/mm$^3$):

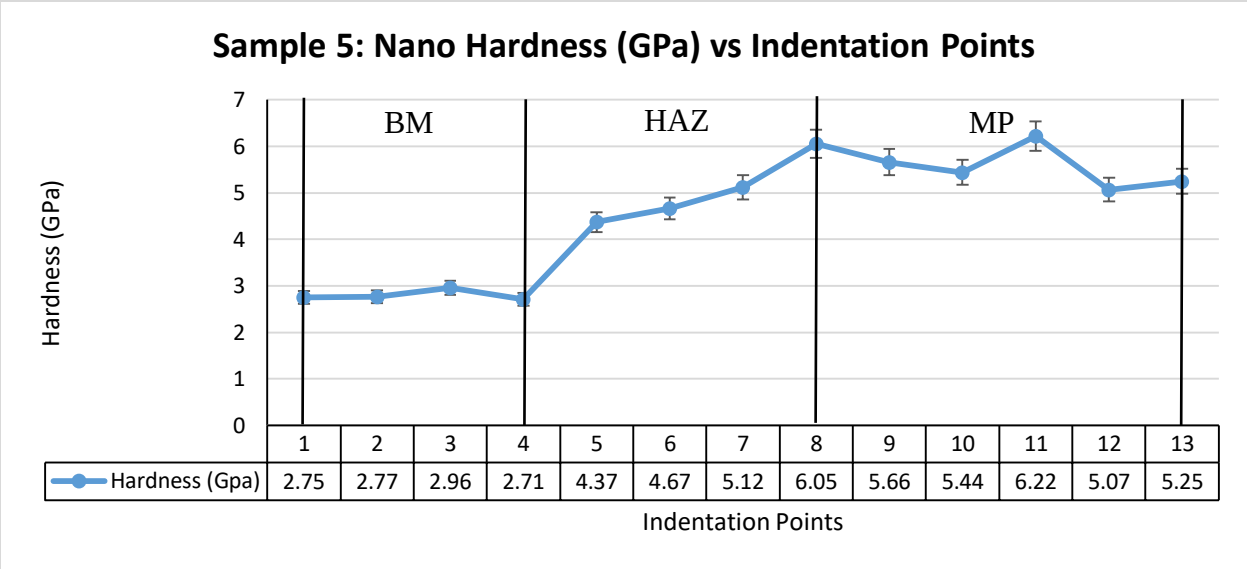


**Figure 48:** Nano hardness of laser treated sample having ED = 300 J/mm$^3$ and defocus of 10mm

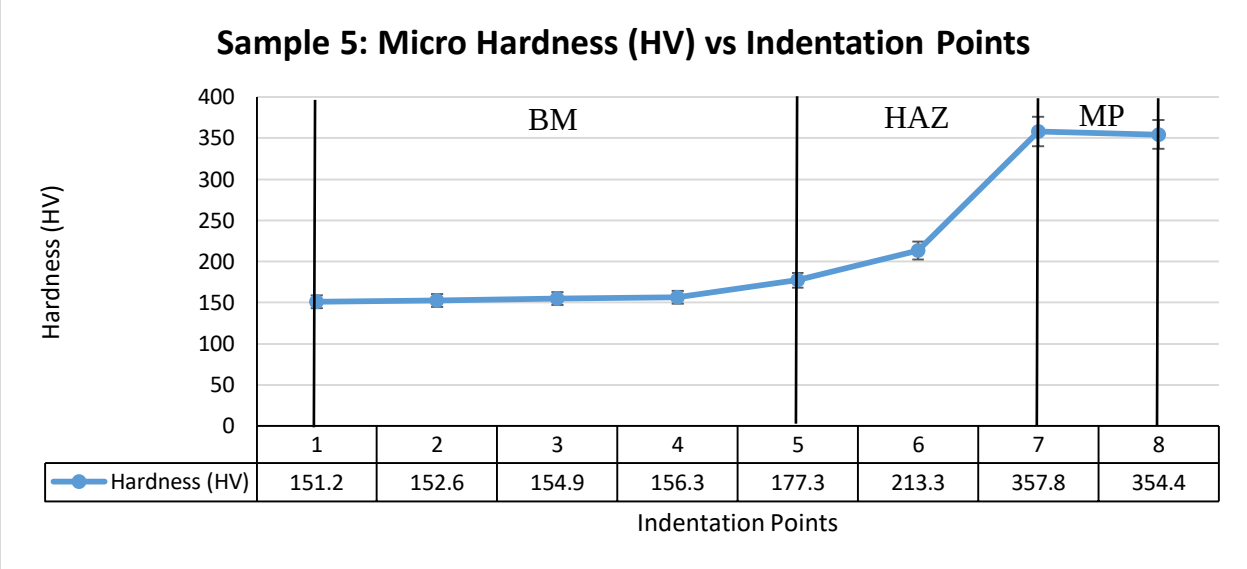


**Figure 49:** Micro hardness of laser treated sample having ED = 300 J/mm$^3$ and defocus of 10mm

Figure 48 is similar to the figure 36 except total indentation points taken in the figure 48 were 13, one more than in the figure 36. The first 4 points lied in BM, next 4 in HAZ and last 5 in MP.

Figure 49 is similar to the figure 37 except total indentation points taken in the figure 49 were 8 due to decrease in depth of MP in the figure 50 as compare to its depth in the figure 37. The first 5 points lied in the BM, next 2 in HAZ and last 1 in MP. There was only one point in MP because of low depth of MP and larger indentation size of micro indenter.

The overall hardness trend in the figure 48 and 49 was similar, the difference between both figures was of total indentation points and it was because of the indenter size difference in micro indenter and nano indenter. The BM in both figures showed constant value of hardness considering low fluctuation in hardness as insignificant in BM. The hardness value increased significantly in HAZ area. The interface of HAZ and MP had high value of hardness as compare to the center of the MP where cooling rate was lower than that of cooling rate at the interface. The high value of hardness in MP near its interface with HAZ showed the material cooled rapidly there because of its interaction with solid phase. The hardness trend in the solidification process was similar to the hardness trend in the figure 48 and 49 [12].

#### 4.10.4.1 Optical Microscopy:

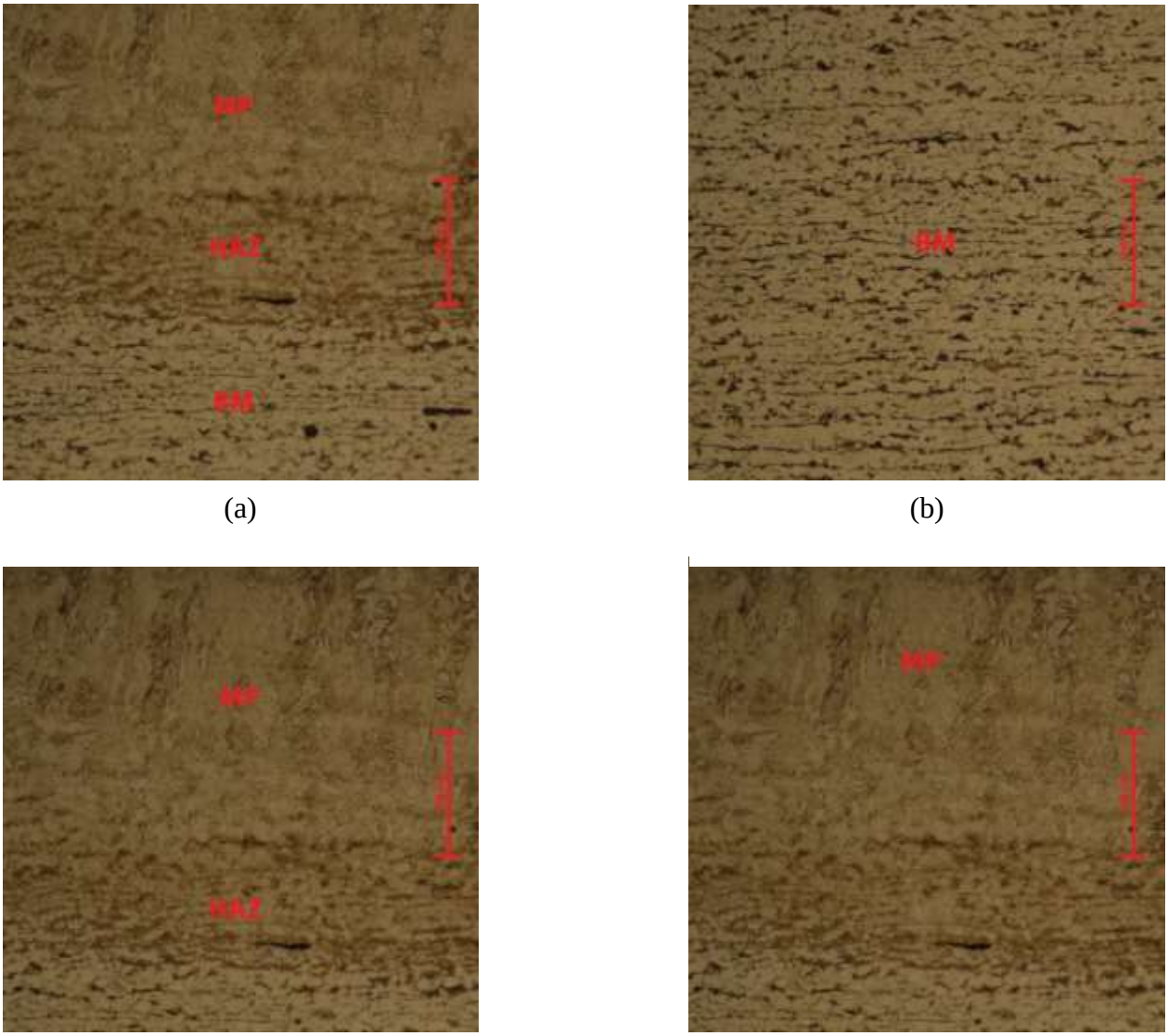


(a) (b)

(c) (d)

**Figure 50:** Microstructure of laser treated sample a) BM, HAZ & MP, b) BM c) HAZ & MP d) MP

Figure 50 shows the microstructure of laser treated sample having ED of 300 J/mm$^3$ and defocus of 10mm. It was similar to the figure 39 in which HAZ and MP had grain refinement which was expected to increase the toughness of the HAZ and MP. The improved toughness was expected to increase the resistance to crack propagation of the analyzed sample. The improved toughness of the sample in HAZ and MP was expected to improve the fatigue life of the sample.

## 4.11 Graph with different ED but same defocus of 2mm:

### 4.11.1 Sample 1 (ED = 75 J/mm$^3$, DF = 2mm):

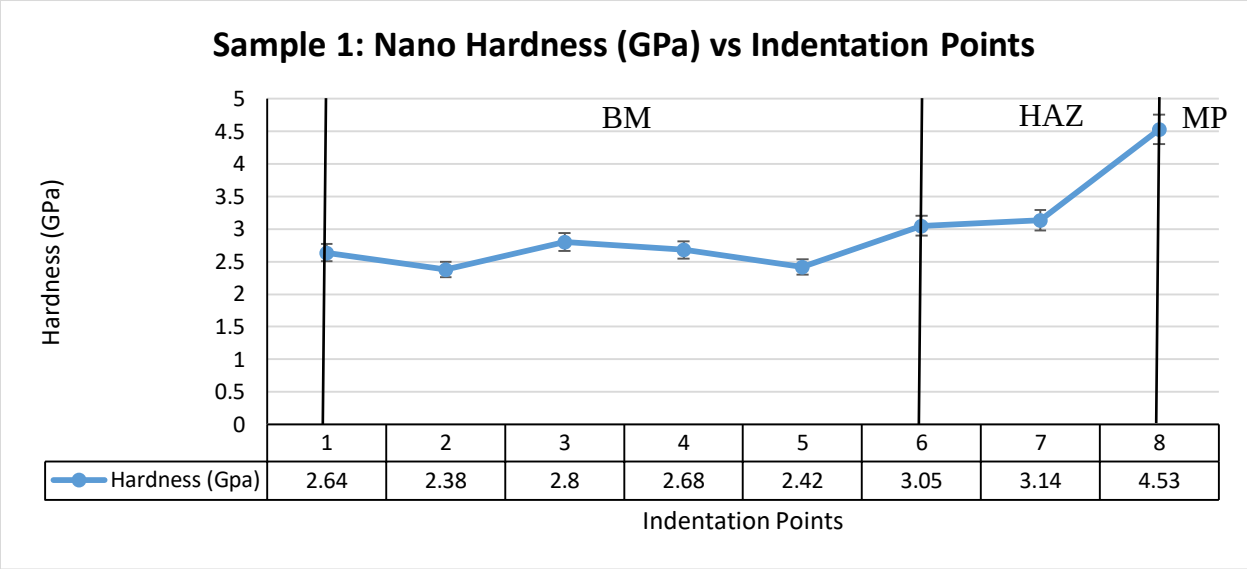


**Figure 51:** Nano hardness of laser treated sample having ED = 75 J/mm$^3$ and defocus of 2mm

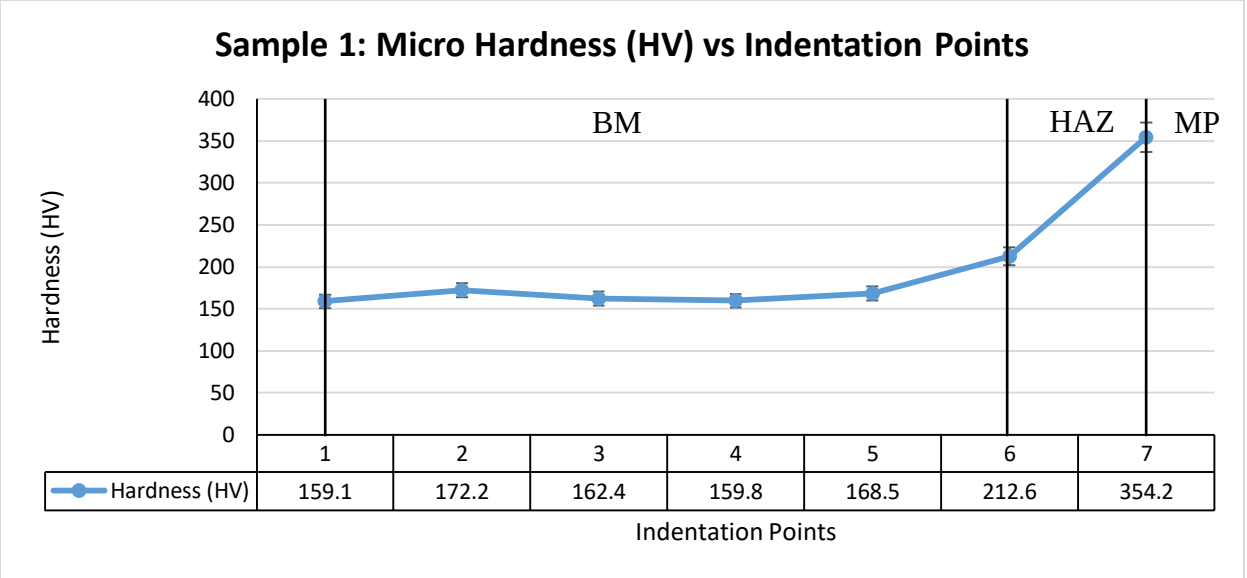


**Figure 52:** Micro hardness of laser treated sample having ED = 75 J/mm$^3$ and defocus of 2mm

Figure 51 is similar to the figure 36 except the total number of indentation points in the figure 51 were 8. The MP was considered to be insignificant because of its low depth. There were only two areas in the figure 51; BM and HAZ. The first 6 indents were made on BM and next 2 on HAZ

Figure 52 is similar to the figure 38 except the number of indentations. The figure 52 had total 7 number of indentation points in which first 6 lied in BM and next 1 in HAZ. There was no indentation in MP because its depth was insignificant to make a micro indent in it.

The overall trend of hardness in the figure 51 and figure 52 was same. The hardness values in BM were considered constant due to insignificant fluctuations in the values. The significant change in value of hardness was observed in the HAZ area and reached its maximum value at the interface of HAZ and MP. The hardness in the MP was not captured due to low depth of MP. The micro indenter and nano indenter slipped at the MP and was at the risk of breakage so the measurement was stopped. The trend of hardness in the figure 51 and 52 followed the hardness trend of solidification process [12].

#### 4.11.1.1 Optical Microscopy:

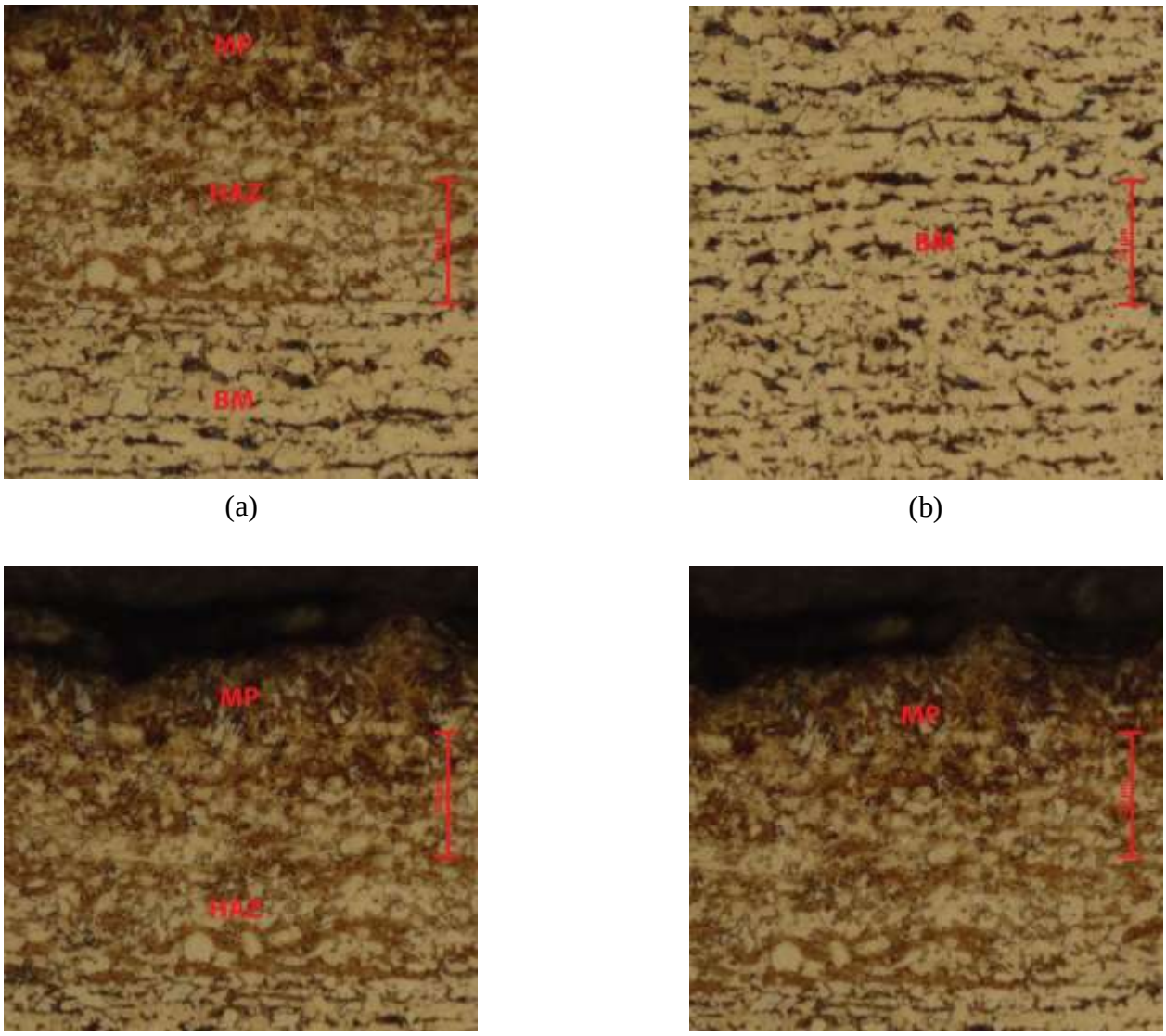


(a) (b)

(c) (d)

**Figure 53:** Microstructure of laser treated sample a) BM, HAZ & MP b) BM c) HAZ & MP d) MP

Figure 53 shows the microstructure of the laser treated sample having ED of 75 J/mm$^3$ and defocus of 2mm. The MP area was very low which can be visualized in the figure 53, part d and HAZ had more area as compare to the MP. The grain refinement can be seen visually in both HAZ and MP which increased the toughness of the sample at those areas. The increase in toughness was desirable to improve the crack resistance and to improve fatigue life of a sample.

### 4.11.2 Sample 2 (ED = 150 J/mm$^3$, DF = 2mm):

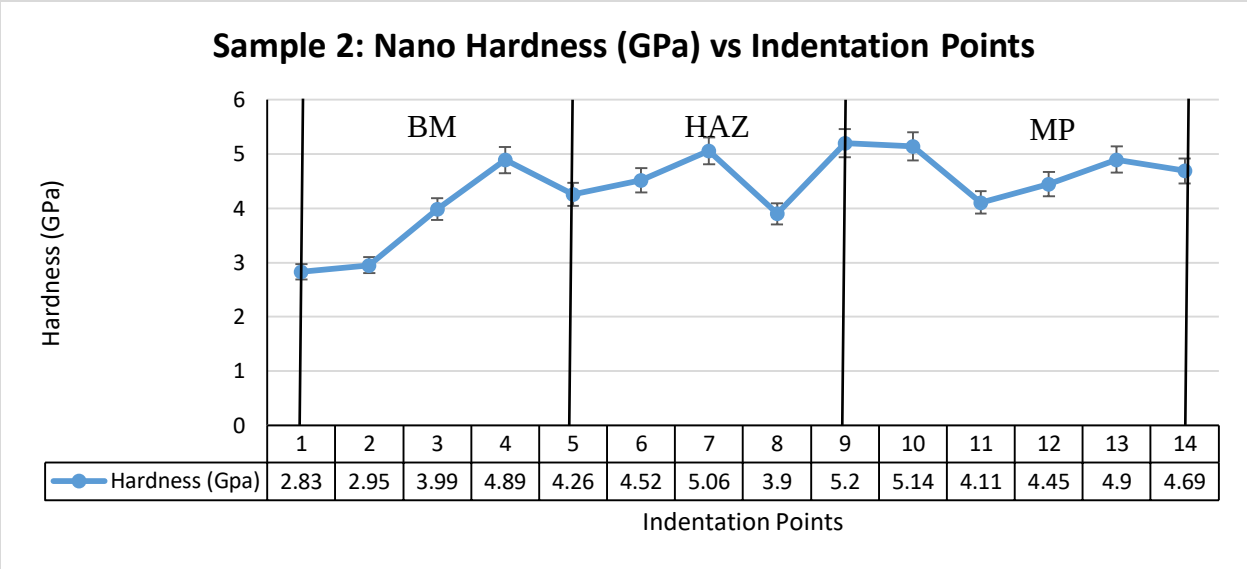


**Figure 54:** Nano hardness of laser treated sample having ED = 150 J/mm$^3$ and defocus of 2mm

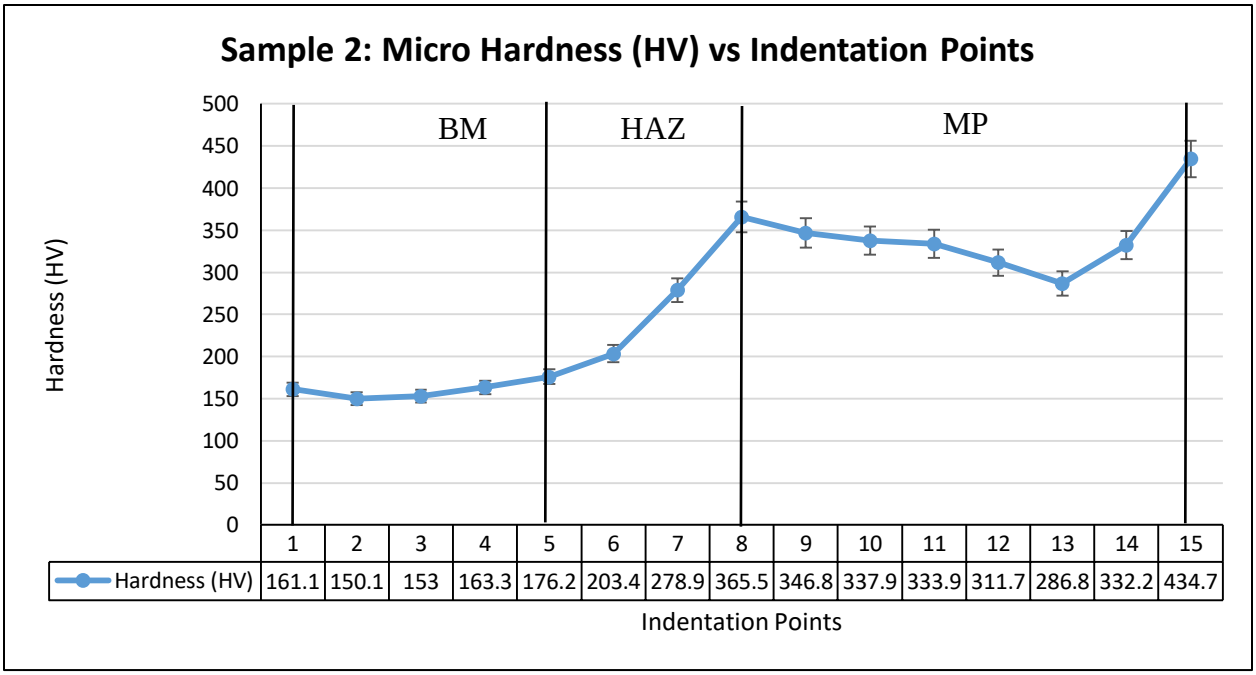


**Figure 55:** Micro hardness of laser treated sample having ED = 150 J/mm$^3$ and defocus of 2mm

Figure 54 is similar to the figure 36 except the total indentation points in the figure 54 were 14. The first 5 points were in BM, next 4 in HAZ and last 5 in MP.

Figure 55 is similar to the figure 37 except total indentation points taken in the figure 55 were 15. The first 5 points lied in BM, next 3 in HAZ and last 7 in MP.

The overall trend of hardness in the figure 54 and 55 was similar in HAZ and MP area but different in BM. The value of hardness in the figure 54 in BM area had large fluctuation, it was due to nano indenter incapable of hitting both phases of the material i.e. ferrite and pearlite. The nano indenter only made indent in harder phases to give high hardness values in BM. The micro indenter instead captured both phases of the material to give constant value of hardness in the BM considering low change insignificant.

The value of hardness increased in HAZ area in both the figures 54 and 55, except at one point in the figure 54, which was due to nano indenter capturing only the hardness of softer phase. The maximum hardness value can be observed at the interface of the HAZ and MP. The area of MP near its interface with HAZ gave high hardness value due to rapid cooling because of its interaction with solid phase. The center of MP showed low hardness because of the low cooling rate which provided the time for the microstructure to be refined. The solidification process [12] after melting followed the hardness trend in the figure 55.

#### 4.11.2.1 Optical Microscopy:

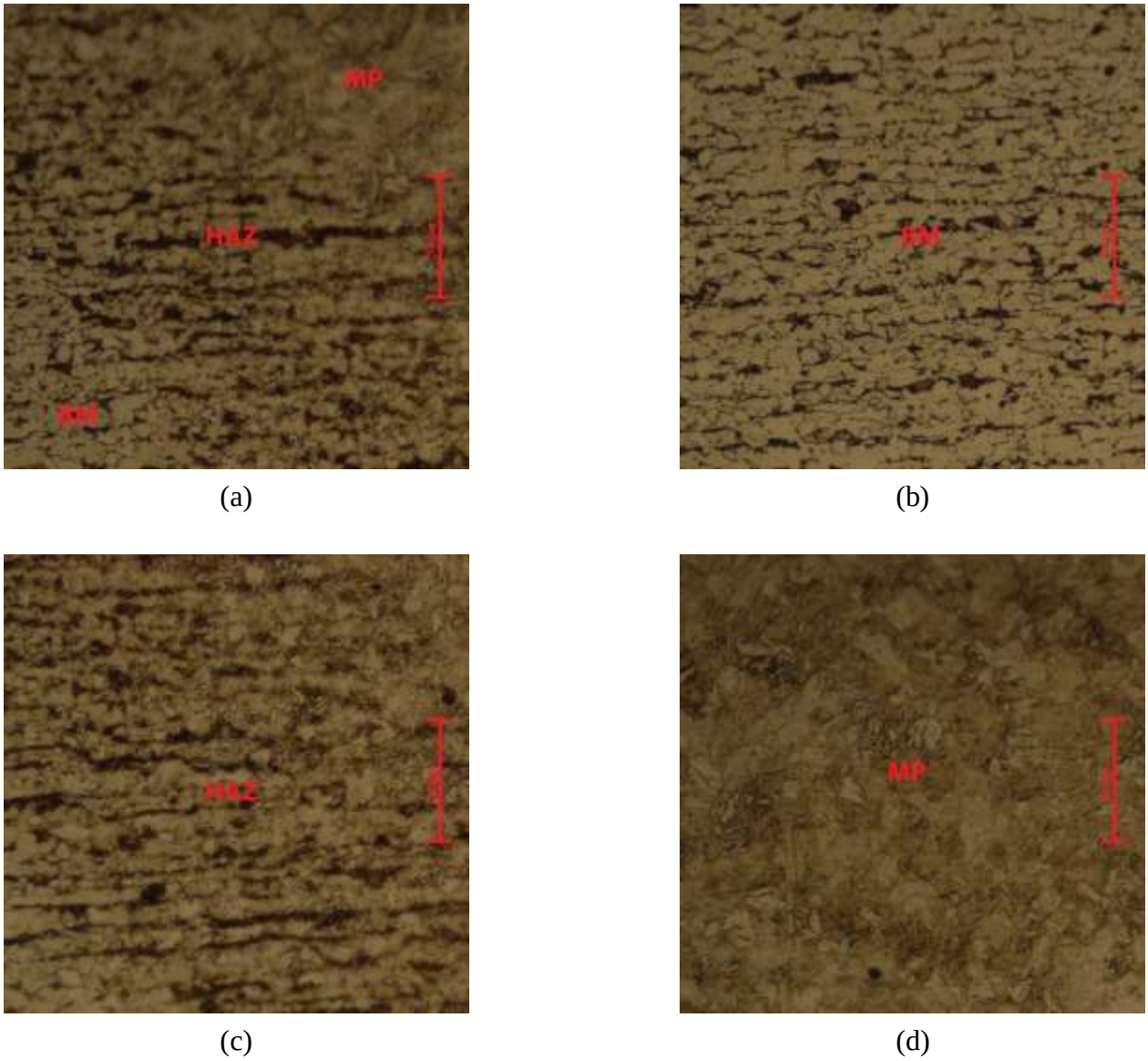


(a) (b)

(c) (d)

**Figure 56:** Microstructure of laser treated sample a) BM, HAZ & MP b) BM c) HAZ d) MP

Figure 56 shows the microstructure of laser treated sample having ED of 150 J/mm$^3$ and defocus of 2mm. It was similar to the figure 38. The martensite, bainite and fine pearlite ferrite microstructures were present in MP depending upon the cooling rates. The percentage of these microstructure in the MP was different from the figure 38. The microstructure in the MP of the figure 56 was expected to increase the toughness of the sample similar to the figure 38. The improved toughness was expected to increase the crack resistance and to improve fatigue life of the sample.

### 4.11.3 Sample 3 (ED = 300 J/mm$^3$, DF = 2mm):

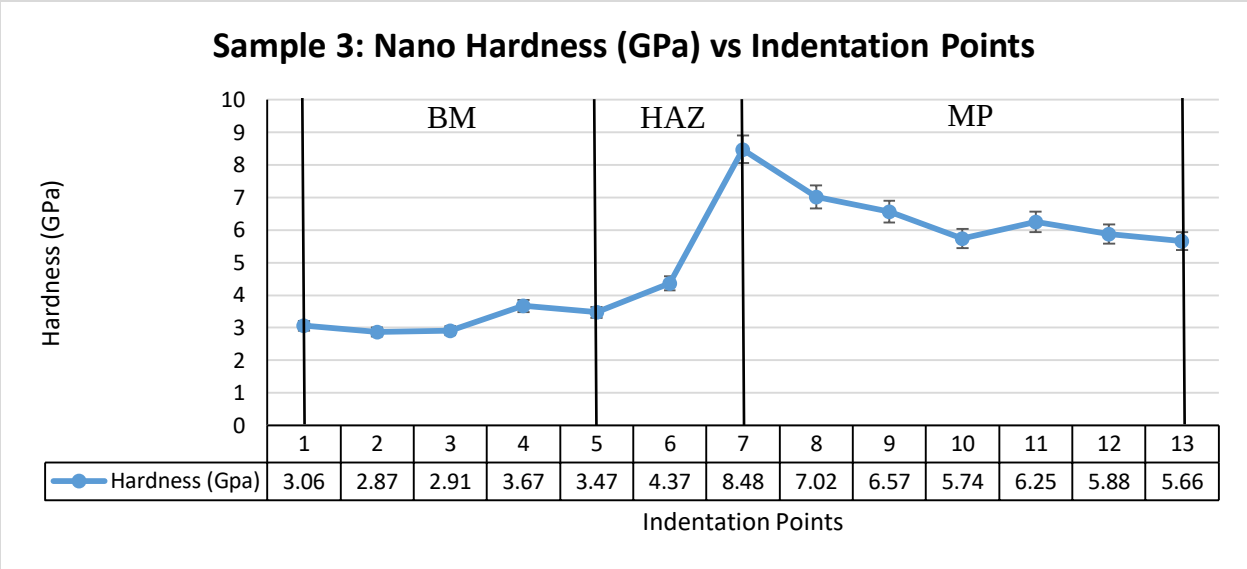


**Figure 57:** Nano hardness of laser treated sample having ED = 300 J/mm$^3$ and defocus of 2mm

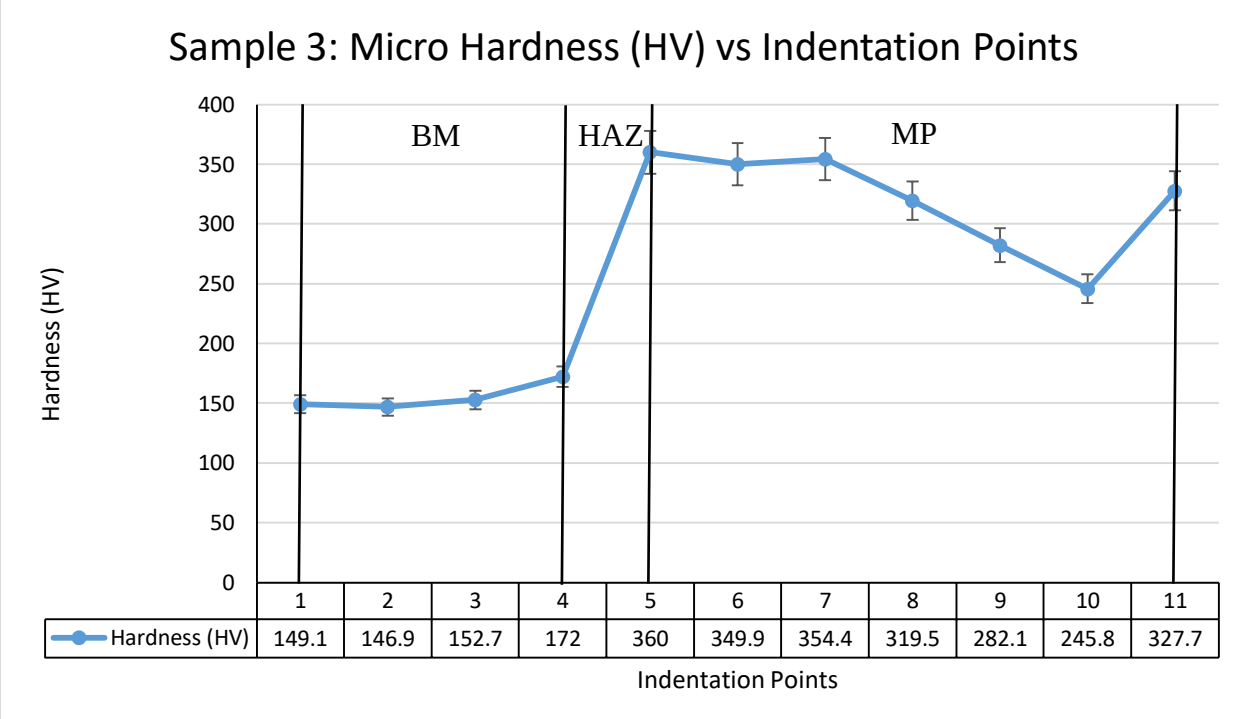


**Figure 58:** Micro hardness of laser treated sample having ED = 300 J/mm$^3$ and defocus of 2mm

Figure 57 is similar to the figure 36 except the number of indentation points in the figure 57 were 13. The first 5 points lied in BM, next 2 in HAZ and last 6 in MP.

Figure 58 is similar to the figure 37 except the number of indentation points in the figure 58 were 11. The first 4 points lied in BM, next 1 in HAZ and last 6 in MP. The difference in

starting position of the micro indenter and nano indenter affected the number of indentation points captured in BM of both figures, 57 and 58. The BM of the figure 57 had 5 points while BM of the figure 58 had 4. The figure 58 had only one point in the HAZ area while figure 57 had 2 points in HAZ area. It was because the micro indenter size was bigger than nano indenter, resulting only one point in HAZ in the figure 58.

The overall trend of the hardness in both of the figures 57 and 58 was similar. The hardness values in the BM was considered constant, the low fluctuation was considered insignificant. The value of hardness increased significantly in the HAZ area and had its maximum value at the interface of HAZ and MP. The area of MP near its interface with HAZ had high hardness values due to rapid cooling because of its interaction with solid phase. The center of the MP area had low hardness due to slow cooling. The solidification process hardness trend [12] was observed to be similar to the overall hardness trend in the figure 57 and 58.

#### 4.11.3.1 Optical Microscopy:

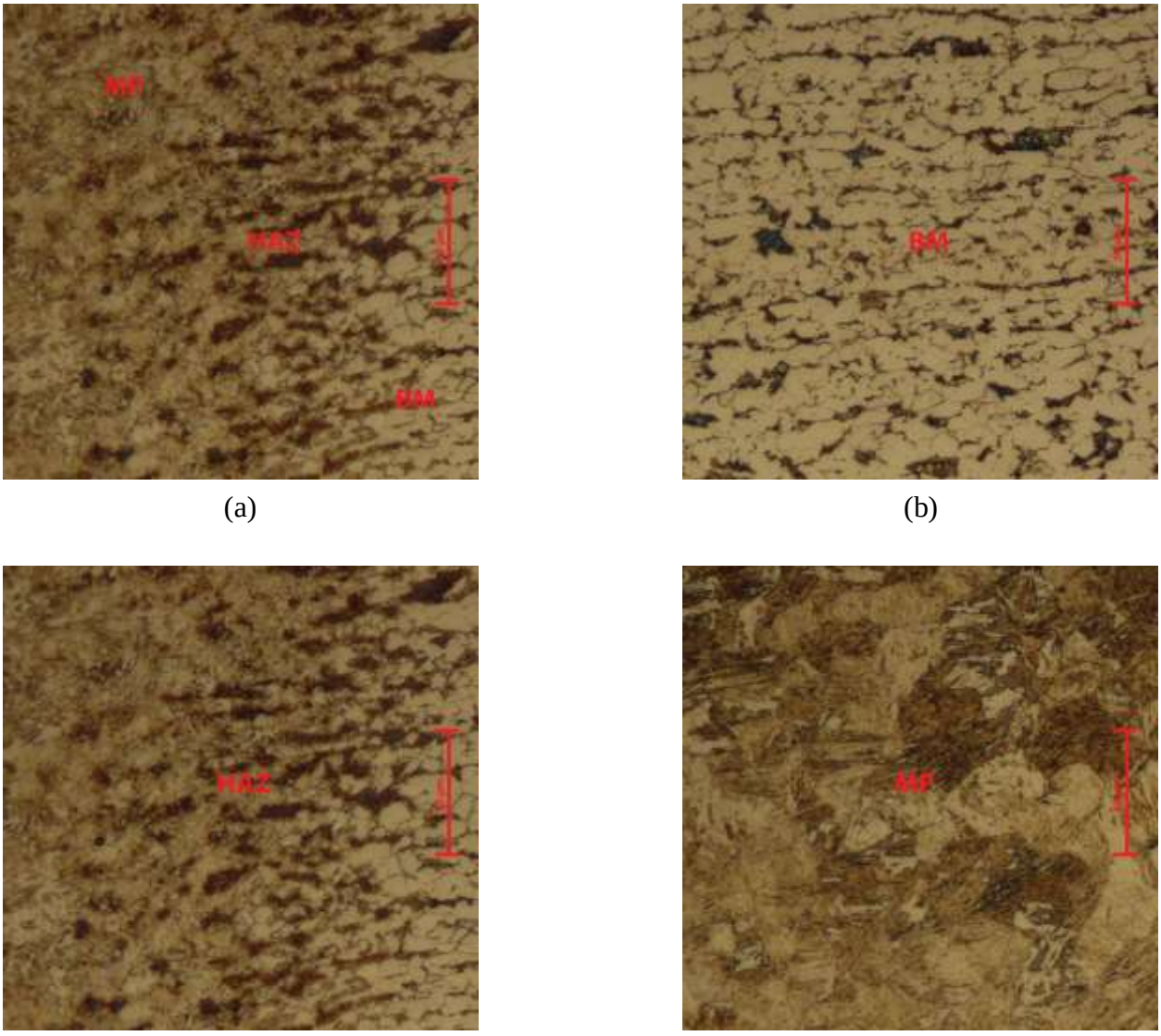


(a) (b)

(c) (d)

**Figure 59:** Microstructure of laser treated sample a) BM, HAZ & MP b) BM c) HAZ d) MP

Figure 59 shows the microstructure of laser treated sample having ED of 300 J/mm$^3$ and defocus of 2mm. It was similar to the figure 38 except the percentage of martensite, bainite and fine pearlite and ferrite in the MP is different. The HAZ had grain refinement similar to that of the figure 38. The toughness in the MP had increased similar to that of the figure 38. The improved toughness was expected to improve fatigue life and to prevent the crack propagation.

### 4.11.4 Sample 4 (ED = 600 J/mm$^3$, DF = 2mm):

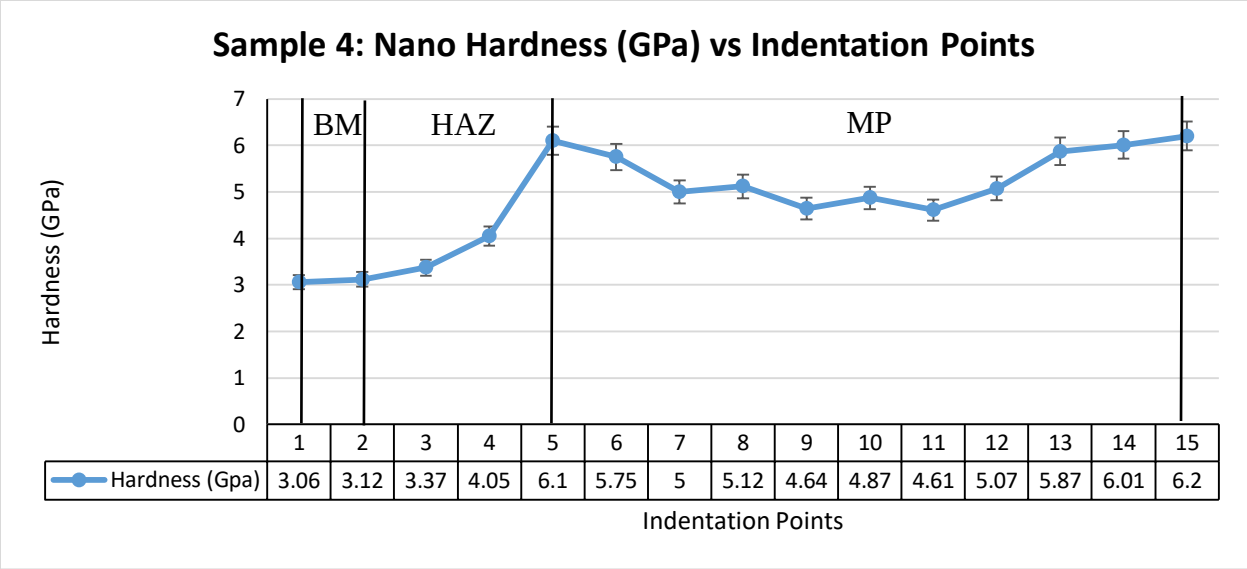


**Figure 60:** Nano hardness of laser treated sample having ED = 600 J/mm$^3$ and defocus of 2mm

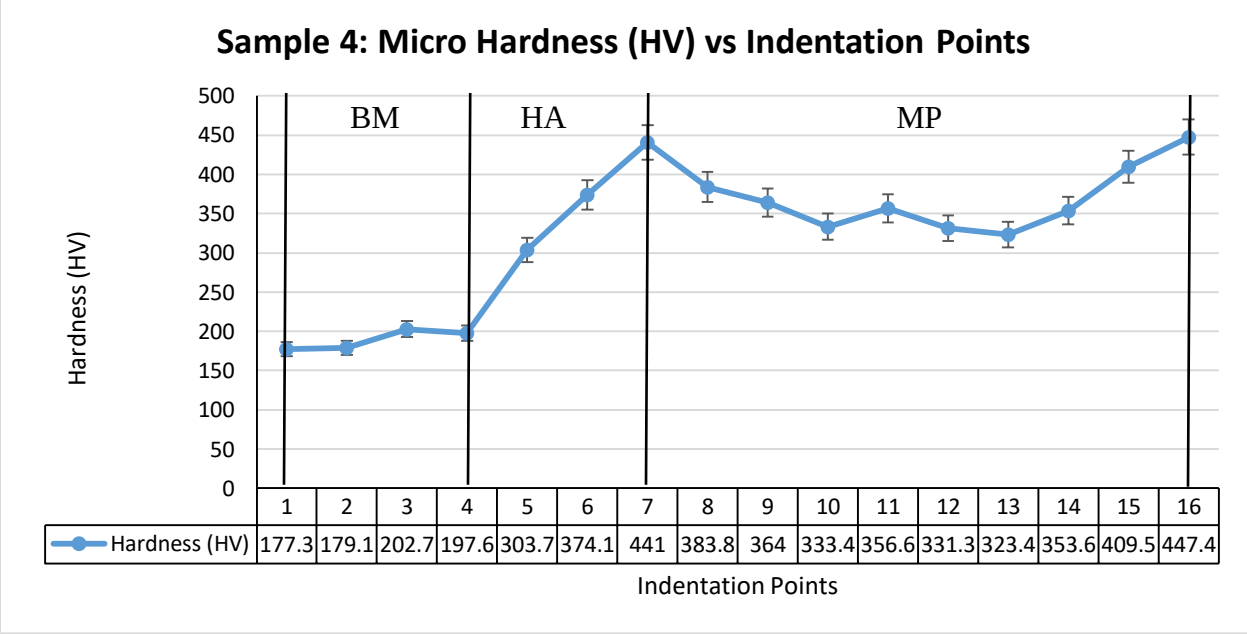


**Figure 61:** Micro hardness of laser treated sample having ED = 600 J/mm$^3$ and defocus of 2mm

Figure 60 is similar to the figure 36 except the total indentation points in the figure 60 were 15. The first 2 points lied in BM, next 3 in HAZ and last 10 points in MP.

Figure 61 is similar to the figure 37 except the number of indentations are 16. The first 4 point lied in BM, next 3 in HAZ and last 9 in MP, The starting position of nano indenter and micro indenter in figure 60 and figure 61 respectively was different and it affected the number of the indentation points lied in BM of both figures, 60 and 61. The figure 60 had 2 points in BM while the figure 61 had 4 points in BM.

The overall trend of hardness in both figures 60 and 61 was same. The BM showed same hardness values as the fluctuation was insignificant. The hardness values increased significantly inside HAZ and showed maximum at its interface with MP. The MP area near its interface with HAZ had high hardness value due to rapid cooling resulted by its interaction with solid phase. The center of the MP showed low hardness due to low cooling rate at it. The solidification process showed hardness similar to the hardness trend in the figure 60 and 61 [12].

#### 4.11.4.1 Optical Microscopy:

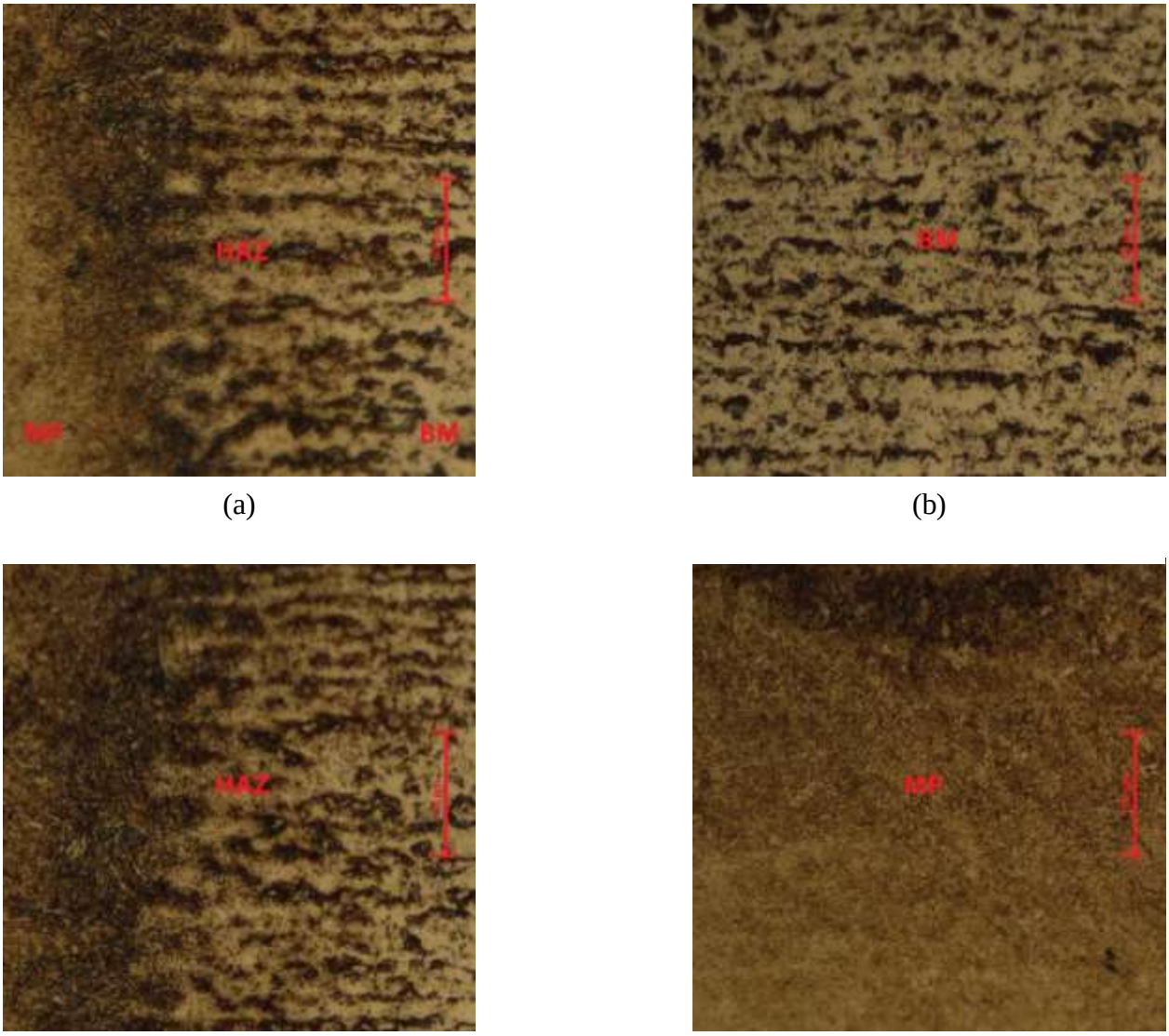


(a) (b)

(c) (d)

**Figure 62:** Microstructure of laser treated sample a) BM, HAZ & MP b) BM c) HAZ d) MP

Figure 62 shows the microstructure of laser treated sample having ED of 600 J/mm$^3$ and defocus of 2mm. This figure is similar to the figure 38. The MP consisted of martensite, bainite and fine pearlite ferrite microstructure similar to the figure 38. The HAZ had grain refinement similar to the figure 38. The toughness was increased due to grain refinement as that of the figure 38. The increased toughness was expected to improve the fatigue resistance and fatigue life.

# CHAPTER 5: CONCLUSION

The laser re-melting of the material at different laser parameters produced different depths of melt pool which can be used to prevent the crack of different depths. The focus of the laser beam was determined by the microscopic study of laser melt pool in different samples. The focused laser beam provided the maximum melt pool depth and minimum kerf width at a certain laser energy density. The micro and nano hardness were performed to understand the change in value of hardness at laser processed area as compare to the base material. The micro and nano hardness results concluded the hardness in the HAZ and MP area was greater than the hardness in the BM. The microstructural study showed the grain refinement and phase transformation at the laser processed area. The grain refinement in HAZ and MP provided better toughness than the BM, resulting in better resistance against the crack propagation. It was expected to increase the fatigue performance and to increase the service life of the cracked material. This study can be used to prevent the crack propagation in the fatigue cracked material.

# REFERENCES


[1] Fatigue Properties, NDT resource center, 2019. [Online]. Available: https://www.nde-ed.org/EducationResources/CommunityCollege/Materials/Mechanical/Fatigue.htm

[2] Manual for Repair and Retrofit of Fatigue Cracks in Steel Bridges, Federal Highway Administration, Washington, D.C., USA, 2013, pp. 19-38.

[3] Y. TAN, G. WU, J.-M. YANG and T. PAN, "Laser shock peening on fatigue crack growth behaviour of aluminium alloy," in Fatigue & Fracture of Engineering Materials & Structures, FFEMS, vol. 27, Aug. 2004, pp. 649-656.

[4] J.C. Betts, "Laser surface modification of aluminium and magnesium alloys," in Surface Engineering of Light Alloys, Cambridge, England: WP, ch. 13, 2010, pp. 444-474.

[5] R. Dexter, R. Fitzpatrick, and D. St. Peter, "Fatigue Strength and Adequacy of Fatigue Crack Repairs," Ship Structure Committee, Washington, D.C., USA, Rep. SSC 425, 2003.

[6] Roy, S., Fisher, J., and Yen, B. "Fatigue Resistance of welded details enhanced by ultrasonic impact treatment (UIT)." in International Journal of Fatigue, vol. 25, Sept. 2003, pp.1239-1247.

[7] Md. Shafiul Ferdous, Kaito Naka, Chobin Makabe and Tatsujiro Miyazaki, "A review of simple methods for arresting crack growth," in Advanced Materials Research, vol. 1110, Mar. 2015, pp. 185 – 190.

[8] K.Ding, L.Ye, "General Introduction," in Laser Shock Peening, Performance and Process Simulation, Cambridge, England: WP, ch. 1, 2006, pp. 1-6.

[9] Chenna Krishna, S., Karthick, Abhay K. Jha, Bhanu Pant & Roy M. Cherian, "Effect of Hot Rolling on the Microstructure and Mechanical Properties of Nitrogen Alloyed Austenitic Stainless Steel," in Journal of Materials Engineering and Performance, JMEP, vol. 27, Apr. 2018, pp. 2388–2393.

[10] Yuelong Yu , Min Zhang , Yingchun Guan , Peng Wu, Xiaoyu Chong , Yuhang Li and Zhunli Tan, "The Effects of Laser Remelting on the Microstructure and Performance of Bainitic Steel," in MPDI Metals, vol. 9, Aug. 2019.

[11] Mushtaq Albdiry, "Investigation on Mechanical Properties of Austenitic Stainless Steel Pipes Welded by TIG Method," in Journal of University of Babylon, Engineering Sciences, vol. 26 no. 1, Dec. 2018.

[12] Seshu Kumar, B. Ravi Kumar, G.L. Datta, V.R. Ranganath, "Effect of microstructure and grain size on the fracture toughness of a micro-alloyed steel," in Materials Science & Engineering A 527, Feb. 2010, pp. 954-960.

[13] Austenite Martensite Bainite Pearlite and Ferrite Structures, The Welding Institute, TWI, 2020. [Online]. Availabale: https://www.twi-global.com/technical-knowledge/faqs/faq-

what-are-the-microstructural-constituents-austenite-martensite-bainite-pearlite-and-ferrite.

[14] Elena Pereloma and David V. Edmonds, Phase Transformations in Steels, vol. 2, Cambridge, England: WP, 2012.

[15] C.Garcia-MateoF.G.Caballero, "Advanced High Strength Bainitic Steels," in Comprehensive Materials Processing, vol. 1, Amsterdam, Netherlands: Elsevier, 2014, pp. 165-190

[16] Gourgues, A. F., H. M. Flower, T. C. Lindley, "Electron Backscattering Diffraction Study of Acicular Ferrite, Bainite, and Martensite Steel Microstructures," in Materials Science and Technology, Jul. 2013, pp.26–40.

[17] J. M. Rodriguez-Ibabe, "The Role of Microstructure in Toughness Behaviour of Microalloyed Steels," in Material Science Forum, vol. 284–286, Jun. 1998, pp. 51–62.

[18] S. Zinelis and W. Brantley, "Fracture Toughness," in Orthodontic Applications of Biomaterials, Cambridge, England: WP, ch 3, sec 4, 2017, Page 66.

[19] Adrian P. Mouritz, "Fracture toughness properties of aerospace materials," in Introduction to Aerospace Materials, Cambridge, England: WP, ch. 19, 2012, pp. 454 – 468.

[20] Standard Specification for Pressure Vessel Plates, Carbon Steel, for Moderate- and Lower-Temperature Service, ASTM A516 / A516M-17, ASTM International, West Conshohocken, PA, 2017, www.astm.org.

[21] Laser, Physics and Radio Electronics, 2015. [Onilne]. Available: https://www.physics-and-radio-electronics.com/physics/laser/ndyaglaser.html

[22] S Kumar, "Selective Laser Sintering/Melting," in Comprehensive Materials Processing, vol. 10, Amsterdam, Netherlands: Elsevier, 2014, Page 95-101.

[23] Labs, National University of Science and Technology H-12 Islamabad Pakistan, 2020. [Online]. Available: http://www.nust.edu.pk/INSTITUTIONS/Schools/SMME/dmrc/Pages/Labs.aspx

[24] ASM International, Metallography and microstructure, vol.9, Cleveland, Ohio, USA: ASM International, 2004.

[25] iMicro Nanoindenter, NANOMECHANICS INC., 2015. [Online]. Available: http://nanomechanicsinc.com/imicro/

[26] Thai-Hoan Pham, Seung-Eock Kim, "Nanoindentation for investigation of microstructural compositions in SM490 steel weld zone," in Journal of Constructional Steel Research, Jul. 2015, pp. 40–47.

[27] ASM International, Properties and Selection: Irons, Steels, and High-Performance Alloys, vol.1, ASM International 10th Ed. Cleveland, Ohio, USA: ASM International, 1990.

[28] Operating Manual, Micro Hardness Tester 401/402MVD, WOLPERT Measuring Equipment Co., Shanghai, China, 2013, pp. 1-32.

[29] Interpretation of the Microstructure of Steels, H. K. D. H. Bhadeshia, University of Cambridge, 2008. [Online]. Available: https://www.phase-trans.msm.cam.ac.uk/2008/Steel_Microstructure/SM.html

[30] Hai QIU, Toshihiro HANAMURA and Shiro TORIZUKA, "Influence of Grain Size on the Ductile Fracture Toughness of Ferritic Steel," ISIJ International, vol. 54, Jan. 2014, pp. 1958-1964.